

1 **Bayesian estimation of past astronomical frequencies, lunar distance, and length of**
2 **day from sediment cycles**

3 **A. Malinverno¹ and S. R. Meyers²**

4 ¹Lamont-Doherty Earth Observatory of Columbia university, Palisades, NY 10964.

5 ²Department of Geoscience, University of Wisconsin–Madison, Madison, WI 53706.

6
7 Corresponding author: Alberto Malinverno (alberto@ldeo.columbia.edu)

8
9 **Key Points:**

- 10 • Two updated methods for Bayesian astrochronology presented: TimeOptB,
11 TimeOptBMCMC
- 12 • TimeOptB estimates axial precession frequency (k) and sedimentation rate (u) from
13 cyclostratigraphic data
- 14 • In addition, TimeOptBMCMC estimates Solar system g -frequencies and s -frequencies
15 from cyclostratigraphic data

18 **Abstract**

19 Astronomical cycles recorded in stratigraphic sequences offer a powerful data source to estimate
20 Earth's axial precession frequency k , as well as the frequency of rotation of the planetary
21 perihelia (g_i) and of the ascending nodes of their orbital planes (s_i). Together, these frequencies
22 control the insolation cycles (eccentricity, obliquity and climatic precession) that affect climate
23 and sedimentation, providing a geologic record of ancient Solar system behavior spanning
24 billions of years. Here we introduce two Bayesian methods that harness stratigraphic data to
25 quantitatively estimate ancient astronomical frequencies and their uncertainties. The first method
26 (TimeOptB) calculates the posterior probability density function (PDF) of the axial precession
27 frequency k and of the sedimentation rate u for a given cyclostratigraphic data set, while setting
28 the Solar system frequencies g_i and s_i to fixed values. The second method (TimeOptBMCMC)
29 applies an adaptive Markov chain Monte Carlo algorithm to efficiently sample the posterior PDF
30 of all the parameters that affect astronomical cycles recorded in stratigraphy: five g_i , five s_i , k ,
31 and u . We also include an approach to assess the significance of detecting astronomical cycles in
32 cyclostratigraphic records. The methods provide an extension of current approaches that is
33 computationally efficient and well suited to recover the history of astronomical cycles, Earth-
34 Moon history, and the evolution of the Solar system from geological records. As case studies,
35 data from the Xiamaling Formation (N. China, 1.4 Ga) and ODP Site 1262 (S. Atlantic, 55 Ma)
36 are evaluated, providing updated estimates of astronomical frequencies, Earth-Moon history, and
37 secular resonance terms.

38

39 **Plain Language Summary**

40 Earth's transit through our Solar system is ever evolving, and so are such seemingly unwavering
41 planetary characteristics as the number of hours in a day. For example, it is well known that the
42 length of the day generally increases with time as Earth's rotation rate decreases from tidal
43 interactions with our orbiting moon. But the ability to chart out this evolution over the history of
44 the Solar system has been hampered by limitations of both data and theoretical models. This
45 study presents a computational approach to map out the history of Solar system motions and the
46 history of the Earth-Moon system, including the length of a day, by leveraging geological data
47 and astronomical theory within a statistical framework that fully accounts for uncertainties. As
48 such, the approach provides a means to use the geological archive as an astronomical
49 observatory, allowing us to explore Solar system and Earth-Moon dynamics throughout their
50 long history.

51

52 **1 Introduction**

53 Quasiperiodic variations in Earth's orbit and axis of rotation influence the amount of
54 solar radiation received at the Earth's surface, causing climate variations and corresponding
55 changes in sediment deposition, and resulting in cyclic sediment sequences that provide a
56 geologic archive of the astronomical rhythms. Following the groundbreaking discovery that
57 astronomical cycles, or "Milankovitch cycles" (Milanković, 1941), pace the Pleistocene ice ages
58 (Hays et al., 1976), there has been growing interest in the use of astrochronology to date
59 stratigraphic sequences and constrain the geological time scale, as well as their use to evaluate
60 Earth System and Solar System evolution (Hinnov, 2013; Ma et al., 2017; Meyers, 2019; Meyers

61 & Malinverno, 2018; Olsen et al., 2019; Pälike et al., 2004). This study presents a Bayesian
62 inversion approach to quantitatively reconstruct ancient astronomical cycles by linking
63 astronomical theory with geologic observation, building on the framework of Meyers (2015;
64 M15 hereafter) and Meyers and Malinverno (2018; MM18 hereafter).

65 The periods of the most prominent Milankovitch cycles (eccentricity, obliquity and
66 climatic precession) are controlled by fundamental Solar system secular frequencies that describe
67 the frequency of rotation of the planetary orbital perihelia (g_i) and the frequency of rotation of
68 the ascending nodes of their ecliptic planes (s_i), combined with the precession frequency of the
69 Earth's spin axis (k). The periods of eccentricity cycles in the Earth's orbit are determined by
70 differences $g_i - g_j$, while those of the obliquity of the Earth's axis by sums $s_i + k$, and those of
71 climatic precession (precession modulated by eccentricity) by sums $g_i + k$. We list in Table 1 the
72 most important cycles used in the present study. The frequencies g_i and s_i are mostly controlled
73 by the corresponding planet ($i = 1$ for Mercury, 2 for Venus, etc.). The eccentricity and climatic
74 precession cycles in Table 1 depend on the g_i for the five innermost planets, and the obliquity
75 frequencies are a function of the s_i for the four innermost planets and Saturn ($i = 6$); s_5 for Jupiter
76 is zero as a consequence of angular momentum conservation (Fitzpatrick, 2012, p. 180).

77 In principle, ancient sediment records that record Milankovitch cycles can be used to
78 estimate past variations in climatic precession, obliquity and eccentricity, as well as the
79 fundamental frequencies (g_i , s_i) and the axial precession frequency (k) from which they derive.
80 This provides a powerful means to peer into the early history of the Solar System and Earth-
81 Moon system, analogous to a telescope imaging distant stars and galaxies to reconstruct the
82 history of the universe (Meyers & Peters, 2022).

83 It has long been known that tidal friction results in a torque that progressively slows
84 down the Earth rotation and accelerates the Moon, sending it into a higher orbit (e.g., Darwin,
85 1898). In turn, the slowing of the Earth's spin and increasing lunar distance result in an increase
86 in the period of the precession of the Earth's axis and a decrease in the axial precession
87 frequency k . This is a large effect over geologic time scales: models and data indicate that k
88 decreased from ~ 86 arcsec/yr at 1.4 Ga to a present value of ~ 50.5 arcsec/yr (MM18; Farhat et
89 al., 2022). In contrast to k , long-term Solar system calculations show that the fundamental
90 frequencies g_i and s_i did not vary greatly over geologic time (Hoang et al., 2021). The value of k
91 can therefore be estimated from sedimentary records by comparing eccentricity frequencies,
92 which do not depend on k , with climatic precession or obliquity frequencies, which depend on k
93 (see Table 1; MM18; Lantink et al., 2022). Estimates of past values of k can constrain the past
94 history of the Earth's length of day (LOD) and lunar distance, informing models for the
95 evolution of tidal dissipation over geological time scales (e.g., Farhat et al., 2022), and better
96 defining the past values of climatic precession and obliquity frequencies for astronomical
97 timescale development.

98 Sediment records can also give information on past values of the fundamental Solar
99 system frequencies g_i and s_i . For example, Olsen et al. (2019) used a long Newark basin Triassic
100 record (~ 210 Ma) to estimate a period of 1.75 Myr for the $g_4 - g_3$ cycle, compared to its present
101 period of ~ 2.4 Myr. Zeebe and Lourens (2019) calculated a Solar system solution that best fitted
102 the Walvis Ridge Site 1262 record, and noted that their solution contains a shift in the $g_4 - g_3$
103 cycle from a period of ~ 1.5 Myr before 50 Ma to ~ 2.4 Myr (near the present value) afterwards. A
104 similar shift of the $g_4 - g_3$ cycle was observed by MM18, through the analysis of a segment of
105 the Walvis Ridge Site 1262 cyclostratigraphic record around 55 Ma. Because of chaotic

106 dynamics, Solar system solutions calculated starting from the present state diverge considerably
 107 at ages beyond ~ 50 Ma (Laskar, 2020), and at earlier ages the period of $g_4 - g_3$ in these model
 108 results fluctuates in a broad range of 1.5-2.6 Myr (Figure 7 of Olsen et al., 2019). Astronomical
 109 cycles recorded in sediments can constrain the value of this long-term periodicity and identify
 110 which computed solutions are consistent with the past Solar system history.

111

112 **Table 1.** Fundamental frequencies of the Solar system (g_i and s_i), axial precession frequency (k), and
 113 astronomical cycle frequencies (eccentricity, obliquity and climatic precession) used in this study and
 114 their present day values. Present day values of g_i and s_i after Hoang et al. (2021); present day value of k
 115 after Farhat et al. (2022).

116

Astronomical frequencies			
	Frequency (arcsec/yr)	Frequency (cycles/kyr)	Period (kyr)
g_1	5.759	0.0044	225.0
g_2	7.448	0.0057	174.0
g_3	17.269	0.0133	75.0
g_4	17.896	0.0138	72.4
g_5	4.257	0.0033	304.4
s_1	-5.652	-0.0044	229.3
s_2	-6.709	-0.0052	193.2
s_3	-18.773	-0.0145	69.0
s_4	-17.707	-0.0137	73.2
s_6	-26.348	-0.0203	49.2
k	50.468	0.0389	25.7
Eccentricity			
	Frequency (arcsec/yr)	Frequency (cycles/kyr)	Period (kyr)
$g_2 - g_5$	3.191	0.0025	406.2
$g_3 - g_2$	9.821	0.0076	132.0
$g_4 - g_2$	10.448	0.0081	124.0
$g_3 - g_5$	13.012	0.0100	99.6
$g_4 - g_5$	13.639	0.0105	95.0
Obliquity			
	Frequency (arcsec/yr)	Frequency (cycles/kyr)	Period (kyr)
$s_6 + k$	24.120	0.0186	53.7
$s_3 + k$	31.695	0.0245	40.9
$s_4 + k$	32.761	0.0253	39.6
$s_2 + k$	43.759	0.0338	29.6
$s_1 + k$	44.816	0.0346	28.9
Climatic precession			
	Frequency (arcsec/yr)	Frequency (cycles/kyr)	Period (kyr)
$g_5 + k$	54.725	0.0422	23.7
$g_1 + k$	56.227	0.0434	23.0
$g_2 + k$	57.916	0.0447	22.4
$g_3 + k$	67.737	0.0523	19.1
$g_4 + k$	68.364	0.0527	19.0

117

118 Astronomical signals recorded by sediment sequences are superimposed on a sizable
119 background of other variability, due to fluctuations in sediment characteristics that are not related
120 to astronomically-driven climatic cycles (e.g., tectonic, geochemical, or ocean circulation
121 changes that influence sedimentation, diagenetic processes). Unrecognized variations in
122 sedimentation rate and hiatuses in sedimentation will also distort the astronomical signals. A
123 method to estimate reliable values of astronomical frequencies therefore needs to 1) quantify
124 uncertainties in the estimated parameters, and 2) provide a measure of significance of the results,
125 to avoid the false detection of astronomical signals in records that do not contain them (Type I
126 errors; Meyers, 2019; Weedon, 2022).

127 In our previous work, M15 established the TimeOpt method, based on how closely
128 stratigraphic data matched Milankovitch periodicities and the expected eccentricity modulation
129 of precession. The method determined a best-fit value for sedimentation rate for prescribed
130 values of five eccentricity frequencies and three climatic precession frequencies (Table 1 of
131 M15). TimeOpt also assessed the statistical significance of the results by comparing the fit
132 obtained for the stratigraphic data to that calculated for random time series of similar statistical
133 characteristics.

134 To extend the methodology and determine from cyclostratigraphic data past values and
135 uncertainties of the astronomical frequencies, MM18 then developed TimeOptMCMC, a Markov
136 chain Monte Carlo method that performs a random walk in the space of the parameters of interest
137 and samples a posterior probability density function (PDF) of sedimentation rate u , of five Solar
138 system frequencies g_i , and of the axial precession frequency k . The posterior PDF combines a
139 prior PDF of the parameters (from information other than that provided by stratigraphic data) and
140 a likelihood function that quantifies how closely data predicted by the parameters fit the
141 stratigraphic data. However, a drawback of TimeOptMCMC is that it typically requires a
142 computationally expensive initial experimentation phase to set up a proposal distribution for the
143 random walk steps that appropriately samples the posterior PDF of the parameters. Once the
144 proposal PDF is properly ‘tuned’, the method is still computationally expensive in its original
145 implementation, typically requiring days to weeks of simulation for each cyclostratigraphic data
146 set.

147 In the present study, we introduce two modified methods that offer significant
148 improvements over the original M15 and MM18 approaches. TimeOptB (‘B’ for Bayesian)
149 extends the TimeOpt methodology of M15 to calculate the posterior PDFs of both sedimentation
150 rate and axial precession frequency, keeping the Solar system fundamental frequencies fixed to
151 characteristic prior values. The statistical significance (‘ p -value’) of the fit of astronomical
152 cycles to the data is also evaluated. TimeOptBMCMC provides a more complete solution by
153 sampling the posterior PDF of sedimentation rate and of all the astronomical parameters of
154 interest: ten Solar system fundamental frequencies (five g_i and five s_i) and the axial precession
155 frequency k . Compared to the previous version, TimeOptBMCMC implements an adaptive
156 sampling strategy that requires no preliminary set up and is orders of magnitude faster in
157 obtaining a useful sample of the posterior PDF. Both methods also implement updated Bayesian
158 priors for the Solar system fundamental frequencies and the axial precession frequency based on
159 astronomical calculations (Farhat et al., 2022; Hoang et al., 2021), and include improvements in
160 the approach used for likelihood estimation.

161 In the rest of this paper, we first describe the Bayesian formulation to compute the value
 162 of the posterior PDF for any value of the astronomical parameters of interest. We then explain in
 163 detail the two new methods, compare their results for the two data sets examined by MM18
 164 (Xiamaling Formation, N. China, 1.4 Ga and ODP Site 1262, S. Atlantic, 55 Ma), and describe
 165 how to obtain estimates of lunar distance and length of day and their uncertainties from the
 166 posterior PDF of the axial precession frequency. We conclude by discussing strengths and
 167 limitations of our approach and future improvements.

168 **2 Bayesian Formulation**

169 The vector \mathbf{m} of the parameters of interest consists of the sedimentation rate u , five
 170 values of g_i , five values of s_i , and the precession frequency k as in

$$171 \quad \mathbf{m} = [g_1, g_2, g_3, g_4, g_5, s_1, s_2, s_3, s_4, s_5, k, u]. \quad (1)$$

172 The posterior PDF of \mathbf{m} is defined from Bayes rule as

$$173 \quad p(\mathbf{m}|\mathbf{d}) = \frac{p(\mathbf{m})p(\mathbf{d}|\mathbf{m})}{p(\mathbf{d})}, \quad (2)$$

174 where the vector \mathbf{d} consists of N sediment property values (e.g., sedimentologic or geochemical
 175 proxy data) measured at constant increments of stratigraphic depth. The two key terms in
 176 Equation (2) are the prior PDF $p(\mathbf{m})$ and the likelihood function $p(\mathbf{d}|\mathbf{m})$. (The denominator $p(\mathbf{d})$
 177 does not depend on \mathbf{m} and is a normalizing constant that is not relevant for the methods
 178 presented here.) The symbols and acronyms used in this paper are listed in Table 2.

179 **2.1 The Prior PDF**

180 The role of the prior PDF is to limit the space of possible parameters to values that agree
 181 with information other than that provided by the stratigraphic data in \mathbf{d} . As there is no
 182 information on prior correlations between the parameters they are taken as independent, so the
 183 prior PDF of \mathbf{m} is simply the product of the prior PDFs of each parameter as in

$$184 \quad p(\mathbf{m}) = p(g_1) p(g_2) \dots p(g_5) p(s_1) \dots p(s_5) p(k) p(u).$$

185 The prior PDF of sedimentation rate u is defined as a uniform distribution between a
 186 minimum and maximum value. These bounds on a realistic value of u can be based on
 187 independent chronostratigraphic information (e.g., radioisotopic dating, bio- or
 188 magnetostratigraphy) or on the environment of deposition (e.g., from the range of sedimentation
 189 rates determined in similar modern and ancient depositional settings).

190 The prior PDFs for the fundamental Solar system frequencies g_i and s_i are the
 191 distributions obtained by Hoang et al. (2021), determined by running a large number of long-
 192 term astronomical solutions starting from slightly different initial conditions. The PDFs of g_i and
 193 s_i are skew Gaussians with some secondary modes, and their parameters are listed in Table 2 of
 194 Hoang et al. (2021) as a function of geologic time. The prior PDFs of the frequencies g_i and s_i are
 195 illustrated in Figure 1 for ages between the present and 3.3 Ga, a time interval that includes most
 196 stratigraphic records available for astronomical cycle analysis.

197

198
199
200**Table 2.** Symbols and acronyms used in this study.

Symbols	
a	Semi-major axis of lunar orbit
\mathbf{C}_e	Covariance matrix of residuals \mathbf{e}
\mathbf{d}	Vector of measured sediment property data
\mathbf{d}_{pred}	Vector of data predicted by parameters in \mathbf{m}
\mathbf{e}	Vector of residuals $\mathbf{d} - \mathbf{d}_{\text{pred}}$
g_i	Fundamental Solar system frequencies for the rotation of the planetary perihelia
k	Earth's axial precession frequency
\mathbf{m}	Vector of parameters (g_i, s_i, k, u)
N	Number of data points in vector \mathbf{d}
N_{eff}	Effective number of independent observations in vector \mathbf{d}
N_{sim}	Number of simulated random data sets in significance testing
R^2	Squared correlation coefficient
\mathbf{R}_e	Correlation matrix of residuals \mathbf{e}
r_i	Autocorrelation coefficient of residuals \mathbf{e} at lag i
s_i	Fundamental Solar system frequencies for the rotation of the ascending nodes of the orbital planes
u	Sedimentation rate
σ_e^2	Variance of residuals \mathbf{e}
τ	Lag where the autocorrelation of \mathbf{e} reaches zero
ϕ_i	Coefficient of an AR(P) process
ω	Earth's spin rate
Acronyms	
AR(P)	Autoregressive process of order P
ETP	Eccentricity, tilt, and precession
LOD	Length of day
M15	Meyers (2015)
MM18	Meyers and Malinverno (2018)
MAP	Maximum a posteriori
MCMC	Markov chain Monte Carlo
PDF	Probability density function

201
202

203 The changes in the mean value of the prior PDF and uncertainties of the fundamental
204 Solar system frequencies in the past are relatively small, a few percent at most. The frequencies
205 associated with the outer planets (g_5 and s_6) vary the least, followed by g_2 . For example, the
206 Earth eccentricity frequency $g_2 - g_5$ (period ~ 405 ka) has remained nearly constant through
207 geologic time and has been proposed as a stable anchoring cycle in astrochronology (e.g.,
208 Hinnov, 2013; Laskar, 2020; Laskar et al., 2004; Olsen et al., 2019).

209 In contrast, the Earth precession frequency k decreased systematically through time due
210 to tidal energy dissipation. The general trend of k in time can be estimated by modeling tidal
211 effects and/or by interpolating past geological estimates of k (e.g., Berger & Loutre, 1994;
212 Laskar et al., 2004). The most recent study is by Farhat et al. (2022), who calculate past
213 precession frequency from a tidal dissipation model that accounts for changes in the overall

214 continental distribution and Earth spin rate. The actual history of tidal dissipation, however, is
 215 not accurately known, and estimated past values of k have large uncertainties (e.g., Waltham,
 216 2015).

217 We set the prior PDF of k to a normal distribution with a time-dependent mean $\mu_k(t)$ and
 218 standard deviation $\sigma_k(t)$. The prior mean is from a polynomial fit to the past variation of k
 219 calculated by Farhat et al. (2022; see their Figure 6) for ages 0-3.3 Ga, which is

$$220 \quad \mu_k(t) = 50.4677 + 23.1305 t + 13.0658 t^2 - 11.2346 t^3 + 2.4322 t^4,$$

221 where age t is in Ga. This polynomial accounts for the long-term expected variation of k in the
 222 past, excluding some shorter-term fluctuations at ages < 600 Ma; these shorter-term variations
 223 should be confirmed (or not) by stratigraphic data and not imposed a priori. The model of Farhat
 224 et al. (2022) was deliberately not fitted to geological data (see p. 4 of Farhat et al., 2022), and it
 225 is appropriate to use the trend they computed as the prior mean of k .

226 The prior standard deviation of k is based on the uncertainties in the past precession
 227 period given in Waltham (2015). These uncertainties are a conservative estimate based on
 228 substantially different assumptions about the past history of tidal dissipation, and we assume that
 229 they correspond to \pm two standard deviations. By fitting a polynomial to the fractional
 230 uncertainty (uncertainty divided by the mean) of the precession period given by the JavaScript
 231 calculator of Waltham (2015) between the present and 3.3 Ga, we obtained an expression for the
 232 prior standard deviation of k :

$$233 \quad \sigma_k(t) = (0.0962 t - 0.0262 t^2 + 0.0030 t^3) \mu_k(t).$$

234 The resulting prior PDF of k is shown in Figure 1. As our knowledge of the geological history of
 235 k , g_i and s_i improve with future studies, this Bayesian approach is adaptable and the prior PDFs
 236 can be updated.

237 **2.2 The Likelihood Function**

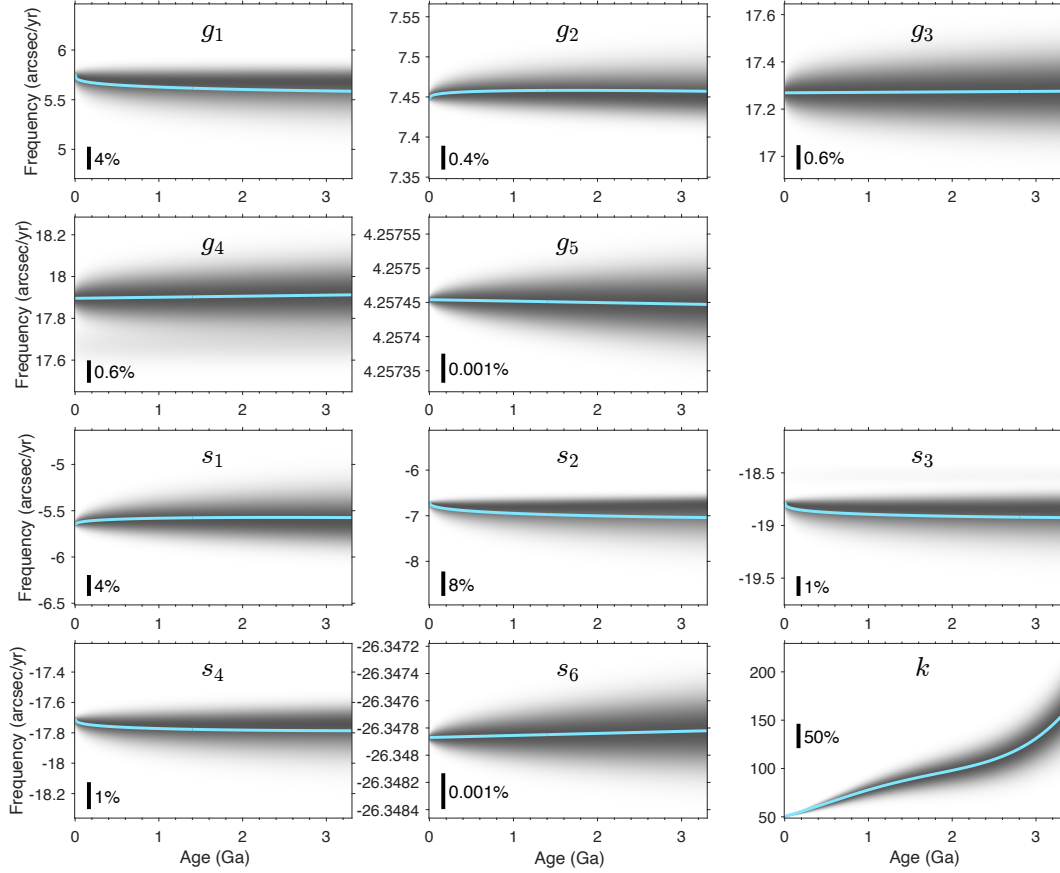
238 The likelihood function quantifies how probable it is to observe the measured
 239 stratigraphic data \mathbf{d} when the parameters have the values in \mathbf{m} , and depends on the difference
 240 between \mathbf{d} and a vector \mathbf{d}_{pred} of data predicted by \mathbf{m} . We define an error or residual vector that is

$$241 \quad \mathbf{e} = \mathbf{d} - \mathbf{d}_{\text{pred}}. \quad (3)$$

242 The value of the likelihood function depends on the overall size of the residuals \mathbf{e} ; the
 243 likelihood of having observed the data \mathbf{d} if the model parameters equal the values in \mathbf{m} will be
 244 greater if the residuals are smaller. Following general practice, the residual vector is assumed to
 245 have a normal distribution and the likelihood is the multivariate normal PDF of the vector of
 246 residuals \mathbf{e} with a mean of zero and a $N \times N$ covariance matrix \mathbf{C}_e . We consider here the general
 247 case where the residuals can be assumed to be second-order stationary, so that their covariance
 248 does not change with position (in our case, stratigraphic depth) and the covariance matrix can be
 249 written as

$$250 \quad \mathbf{C}_e = \sigma_e^2 \mathbf{R}_e,$$

251



252
253

254 **Figure 1.** Prior PDFs of astronomical frequencies shown as gray scale images as a function of age (0-3.5
255 Ga; see the text for details). The blue continuous line shows the prior mean and the black vertical bars
256 display the scale of the overall variations as a percentage of the present value. The Solar system
257 fundamental frequencies g_1 to g_5 , s_1 to s_4 , and s_6 display a much lower variability compared to the
258 systematic decrease with time of the axial precession frequency k .
259

260 where \mathbf{R}_e is a symmetric Toeplitz matrix of correlation coefficients with a unit diagonal and
261 constant off-diagonal entries as in

262

$$\mathbf{R}_e = \begin{bmatrix} 1 & r_1 & r_2 & \dots & r_{N-1} \\ r_1 & 1 & r_1 & \ddots & \vdots \\ r_2 & r_1 & 1 & \ddots & r_2 \\ \vdots & \ddots & \ddots & \ddots & r_1 \\ r_{N-1} & \dots & r_2 & r_1 & 1 \end{bmatrix},$$

263 and r_i is the autocorrelation function of \mathbf{e} at lag i ($-1 < r_i < 1$). If the residuals were
264 uncorrelated, \mathbf{R}_e would equal the identity matrix.

265 TimeOptB and TimeOptBMCMC use two likelihood functions that measure the fit to two
266 kinds of predicted data. The first (“spectral fit” of M15 and MM18) is based on predicted data
267 \mathbf{d}_{pred} obtained by fitting to the observed stratigraphic data cycles of eccentricity, obliquity, and
268 climatic precession given by the astronomical frequencies and sedimentation rate in \mathbf{m} . The
269 second (“envelope fit” of M15 and MM18) is based on predicting the envelope of a bandpass-

270 filtered climatic precession signal with the eccentricity frequencies derived from \mathbf{m} . In both
 271 cases, the residuals in \mathbf{e} are positively correlated. For example, it is well known that stratigraphic
 272 data have a “red noise” character and can be modeled as autoregressive processes with positive
 273 correlations of nearby values (e.g., Mann & Lees, 1996).

274 It is important to account for these correlations in the likelihood function because they
 275 affect the posterior uncertainties of the parameters. Consider a simple case where the parameter
 276 of interest is the mean of the observations, estimated from a sample mean μ as in

$$277 \quad \mu = \frac{1}{N} \sum_{i=1}^N d_i.$$

278 If the residuals $\mathbf{e} = \mathbf{d} - \mu$ have a variance σ_e^2 and are uncorrelated, the likelihood function
 279 of the sample mean would have a variance equal to σ_e^2/N . However, if the residuals are positively
 280 correlated there are fewer than N independent observations. For example, if the autocorrelation
 281 function of the residuals \mathbf{e} decreased from unity at zero lag to a value near zero at a lag τ , the
 282 effective number of independent observations would approximately be

$$283 \quad N_{\text{eff}} \approx N/\tau$$

284 (e.g., Neal, 1993; Priestley, 1981; Zięba, 2010; Zięba & Ramza, 2011). As $N_{\text{eff}} < N$, the sample
 285 mean would have a variance $\sigma_e^2/N_{\text{eff}}$ that is greater than in the case where the residuals were
 286 uncorrelated. If correlations in the data residuals were ignored, the likelihood function would be
 287 artificially concentrated around its mode, causing an underestimation of the uncertainties in the
 288 parameters. This could be a substantial bias; in the example of the sample mean, if the data were
 289 correlated up to a lag $\tau = 9$, ignoring these correlations would underestimate the posterior
 290 uncertainty by a factor of three (measured from the standard deviation).

291 Moreover, when the likelihoods for several data fits are combined, it is important to
 292 account for differences in the correlations of the residuals. In our application, the residuals in the
 293 spectral fit are clearly less correlated than the much smoother residuals in the envelope fit.
 294 Ignoring this difference in the correlations would not properly weigh the importance of each data
 295 fit in constraining the parameters.

296 An outstanding problem in defining the likelihood function in Bayesian inference is that
 297 the variance and autocorrelation of the residuals \mathbf{e} are typically unknown and cannot be
 298 confidently set a priori. On the other hand, the data may be informative about the statistical
 299 properties of the residuals. For example, fitting a few harmonic components as in the spectral fit
 300 will always result in non-zero residuals, and the statistics of these residuals may be used to infer
 301 the residual variance and autocorrelation.

302 One way to extract this information is to follow a hierarchical Bayes strategy (Gelman et
 303 al., 2004; Malinverno & Briggs, 2004) by adding σ_e^2 and parameters that define the correlation
 304 matrix \mathbf{R}_e to the unknowns of the problem as “hyperparameters.” The original TimeOptMCMC
 305 of MM18 implemented this strategy by adding to the parameter vector two hyperparameters for
 306 each of the spectral and envelope fit: the variance of the data residuals σ_e^2 and the coefficient ϕ_1
 307 of an autoregressive process of order 1 that defined their autocorrelation. These four
 308 hyperparameters were then sampled by MCMC, and the sampled values were used to define the
 309 covariance matrix \mathbf{C}_e when calculating the likelihood at each iteration. The final histogram of the
 310 sampled σ_e^2 and ϕ_1 described their posterior PDFs (Fig. S4, S7, and S10 of MM18).

311 In the updated methodology presented here, we apply an empirical Bayes strategy, where
 312 values of the hyperparameters are estimated from the data (Carlin & Louis, 2000; Casella, 1985).
 313 While hierarchical Bayes fully accounts for the posterior uncertainty of the hyperparameters,
 314 empirical Bayes simplifies the calculations, speeds up the inversion, and can return a posterior
 315 PDF for the parameters in \mathbf{m} that is close to that obtained by hierarchical Bayes (see the
 316 discussion of Figure 9 in Malinverno & Briggs, 2004).

317 The rest of this section describes the form of the likelihood function for the spectral and
 318 envelope fits. Assuming that there are no correlations between the residuals obtained in the two
 319 fits, the total likelihood is simply the product of the spectral and envelope likelihoods.

320 **2.2.1 Likelihood for the Spectral Fit**

321 The spectral fit likelihood is based on modeling the residuals \mathbf{e} in Equation 3 as an
 322 autoregressive process of order 2, or AR(2), as in

$$323 \quad e_i = \phi_1 e_{i-1} + \phi_2 e_{i-2} + w_i, \quad (4)$$

324 where the vector \mathbf{w} is white noise, a sequence of uncorrelated normally distributed values that
 325 have zero mean and a variance σ_w^2 . The AR process exploits the correlations in the vector \mathbf{e} to
 326 predict the i -th value e_i with a linear combination of nearby values, while the driving noise term
 327 w_i accounts for unpredictable random effects. If the time series in \mathbf{e} is adequately modeled by an
 328 AR(2) process, the resulting \mathbf{w} (which can be obtained by solving Equation 4 for w_i) should be
 329 white noise. This can be verified by computing the sample autocorrelation of the estimated \mathbf{w} and
 330 checking that the autocorrelation values are not significantly different from zero for nonzero
 331 lags. Whereas cyclostratigraphic analyses often assume that stratigraphic records can be modeled
 332 as an AR(1) process (e.g., MM18; Mann & Lees, 1996), we found that in several cases an AR(2)
 333 process is necessary to produce a vector \mathbf{w} that is close to white noise. A general description of
 334 AR processes can be found in treatments of time series analysis (Chatfield, 1989; Cox & Miller,
 335 1965; Priestley, 1981).

336 Dettmer et al. (2012) proposed a way to simplify the evaluation of a multivariate normal
 337 likelihood if the residuals \mathbf{e} can be modeled as an AR process. In the AR(2) process (Equation 4),
 338 values e_i can be predicted by e_{i-1} and e_{i-2} plus a driving noise w_i that is uncorrelated. Therefore,
 339 the residuals \mathbf{e} contain a predictable component and a random component \mathbf{w} ; if we subtract the
 340 predictable component of \mathbf{e} , the likelihood function can then be written as the PDF of the
 341 uncorrelated driving noise \mathbf{w} . This simplifies considerably the calculation of the likelihood
 342 because the covariance matrix of \mathbf{w} is diagonal. To complete the calculation of the spectral fit
 343 likelihood, we apply an empirical Bayes strategy and estimate the AR(2) coefficients ϕ_1 and ϕ_2
 344 and the variance σ_w^2 of the driving noise \mathbf{w} from the residuals \mathbf{e} (Andersen, 1974; Burg, 1967;
 345 Ulrych & Bishop, 1975). Details on the calculation of the predicted data in the spectral fit, on the
 346 estimation of ϕ_1 , ϕ_2 , and σ_w^2 , and on the equation for the spectral fit likelihood are in the
 347 Supporting Information.

348 **2.2.2 Likelihood for the Envelope Fit**

349 It seems reasonable to apply the same methodology to the evaluation of the likelihood of
 350 the envelope fit. However, an AR(P) model is not a good representation of the residuals of the
 351 envelope fit, even if the order P is high. The reason is that these residuals \mathbf{e} are the difference of
 352 two low-frequency band-limited signals: the envelope of a filtered climatic precession signal in

353 the data (\mathbf{d} in Equation 3) minus the sum of harmonic components with the periods of
 354 eccentricity (\mathbf{d}_{pred}). Therefore, the residuals in the envelope fit are very smooth and cannot be
 355 well reproduced by an autoregressive process driven by uncorrelated noise.

356 The likelihood of the envelope fit instead uses an effective number of independent
 357 observations $N_{\text{eff}} = N/\tau < N$, based on an estimate of the lag τ where the autocorrelation of the
 358 envelope fit residuals reaches zero (Zięba, 2010; Zięba & Ramza, 2011). Details on the bandpass
 359 filtering to extract the climatic precession signal in the data (Zeeden et al., 2018), on the
 360 calculation of the predicted precession envelope, on the estimation of the lag τ , and on the
 361 equation for the envelope fit likelihood are in the Supporting Information.

362 **3 TimeOptB Methodology**

363 As the Solar system frequencies g_i and s_i do not vary greatly throughout geologic time
 364 (Figure 1), in TimeOptB we fix these frequencies to their prior mean value at the time of
 365 sediment deposition, so that the only variable parameters in \mathbf{m} are the sedimentation rate u and
 366 the axial precession frequency k . The value of the likelihood, prior PDF, and posterior PDF can
 367 then be calculated over a 2-D grid of u and k . The boundaries of this grid can be initially set to
 368 span the range of the prior PDF and can then be narrowed to resolve details of the posterior PDF.

369 Compared to the original TimeOpt of M15, the major enhancements in TimeOptB are
 370 that 1) the axial precession frequency k is not fixed but is a variable that is estimated from the
 371 data and 2) that the Bayesian formulation provides a measure of uncertainty in the values of u
 372 and k consistent with the data.

373 The significance of astronomical cycles inferred from noisy stratigraphic data is an
 374 outstanding issue, and it has been claimed that false detection of such cycles is likely widespread
 375 in existing studies (Weedon, 2022). As done in TimeOpt, we implemented in TimeOptB a simple
 376 Monte Carlo procedure to investigate the statistical significance of the detected astronomical
 377 cycles. The procedure is based on generating a large sample of N_{sim} random simulated data series
 378 that are AR(2) processes with coefficients ϕ_1 and ϕ_2 equal to those estimated from the observed
 379 data for the maximum a posteriori value (MAP) values of u and k . In each of these N_{sim} data sets,
 380 we repeat the TimeOptB procedure for the spectral fit over the range of u and k explored with the
 381 measured data and retain the maximum value of the Pearson R^2 correlation coefficient (the ratio
 382 of the variances of the data predicted by fitting astronomical cycles over the total variance). We
 383 then compare the maximum spectral fit R^2 values obtained in each of the N_{sim} simulated data sets
 384 to the R^2 obtained for the actual data at the MAP values of u and k . (It should be noted that in
 385 each of the simulated data series the maximum R^2 will be obtained for values of u and k that are
 386 different than the MAP values in the measured data.)

387 Following the general philosophy of significance testing (Hacking, 2001) we define a p -
 388 value as the fraction of N_{sim} cases where the R^2 of the simulated data sets is as large or larger
 389 than the R^2 in the measured data. If the data contain significant astronomical cycles, a
 390 comparable fit should only occur rarely in the random simulated data sets and the p -value should
 391 be small. To further investigate astronomical cycle significance, we also repeat the same Monte
 392 Carlo procedure separately for cycles of eccentricity, obliquity, and climatic precession. Whereas
 393 the critical significance test is for all the astronomical cycles, the results of the Monte Carlo
 394 experiment when only one set of cycles is considered will highlight which cycles are most
 395 informative in a particular cyclostratigraphic data set.

396 The accuracy of the p -value estimated in this Monte Carlo procedure will obviously
 397 improve as N_{sim} grows; we suggest $N_{\text{sim}} \geq 1,000$. Even if N_{sim} is large, the estimated p -value is
 398 not assured to be the same in different runs of N_{sim} Monte Carlo simulations. In practice, it may
 399 be the case that no simulated data set reaches the fit level observed for the measured data; in that
 400 case, all that can be concluded from the Monte Carlo experiment is that the p -value is $< 1/N_{\text{sim}}$.

401 **4 TimeOptB example results**

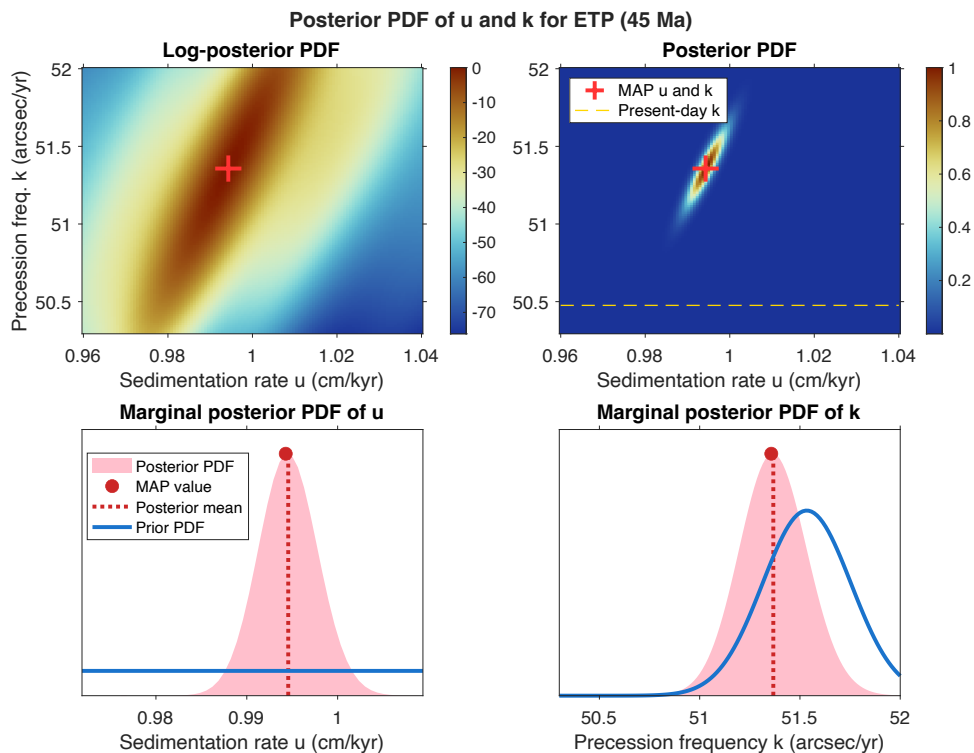
402 **4.1 ETP curve (45 Ma)**

403 To evaluate the efficacy of the TimeOptB approach, we test it against a synthetic data set
 404 that consists of known astronomical signals plus random noise. An ETP astronomical signal is
 405 constructed as the sum of eccentricity, obliquity (tilt), and climatic precession from the solution
 406 of Laskar et al. (2004). The synthetic record consists of 1000 data points spanning a 1 Myr
 407 interval centered on an age of 45 Ma and was converted to depth assuming a sedimentation rate
 408 of 1 cm/kyr. Each of the three astronomical signals was normalized to zero mean and unit
 409 variance before their summation. A time series of AR(1) correlated noise ($\phi_1 = 0.8$) was added to
 410 the astronomical signals to obtain the final synthetic data set. The noise variance was adjusted so
 411 that the variance of the astronomical signals was 0.44 times the total variance (a value of $R^2 =$
 412 0.44 is close to that obtained for the stratigraphic data sets that will be shown later).

413 Images of the log-posterior and posterior PDFs as a function of sedimentation rate u and
 414 axial precession frequency k are shown in Figure 2. The posterior PDF images display a strong
 415 positive correlation between u and k , which is intrinsic to the estimation of astronomical periods
 416 from stratigraphic data. If the stratigraphic data contain a cycle with a distinct spatial wavelength
 417 attributed to an astronomical cycle, the temporal frequency of that cycle will be a function of the
 418 sedimentation rate; if the sedimentation rate were higher, the frequency of the astronomical cycle
 419 will increase correspondingly (see also the discussion).

420 The marginal posterior PDFs of u and k in Figure 2 are obtained by integrating the images
 421 in the vertical and horizontal directions, respectively. The posterior means of u and k (0.995
 422 cm/kyr and 51.367 arcsec/yr) are very close to the sedimentation rate used in the synthetic
 423 example and to the axial precession frequency at 45 Ma in the Laskar et al. (2004) calculations
 424 (which is 51.707 arcsec/yr, from their Equation 40). Notably, if the sedimentation rate were
 425 increased by 0.5% to the exact value of 1 cm/yr, the posterior mean axial precession would
 426 increase by the same amount to 51.624 arcsec/yr, getting even closer to the value expected in the
 427 ETP signal.

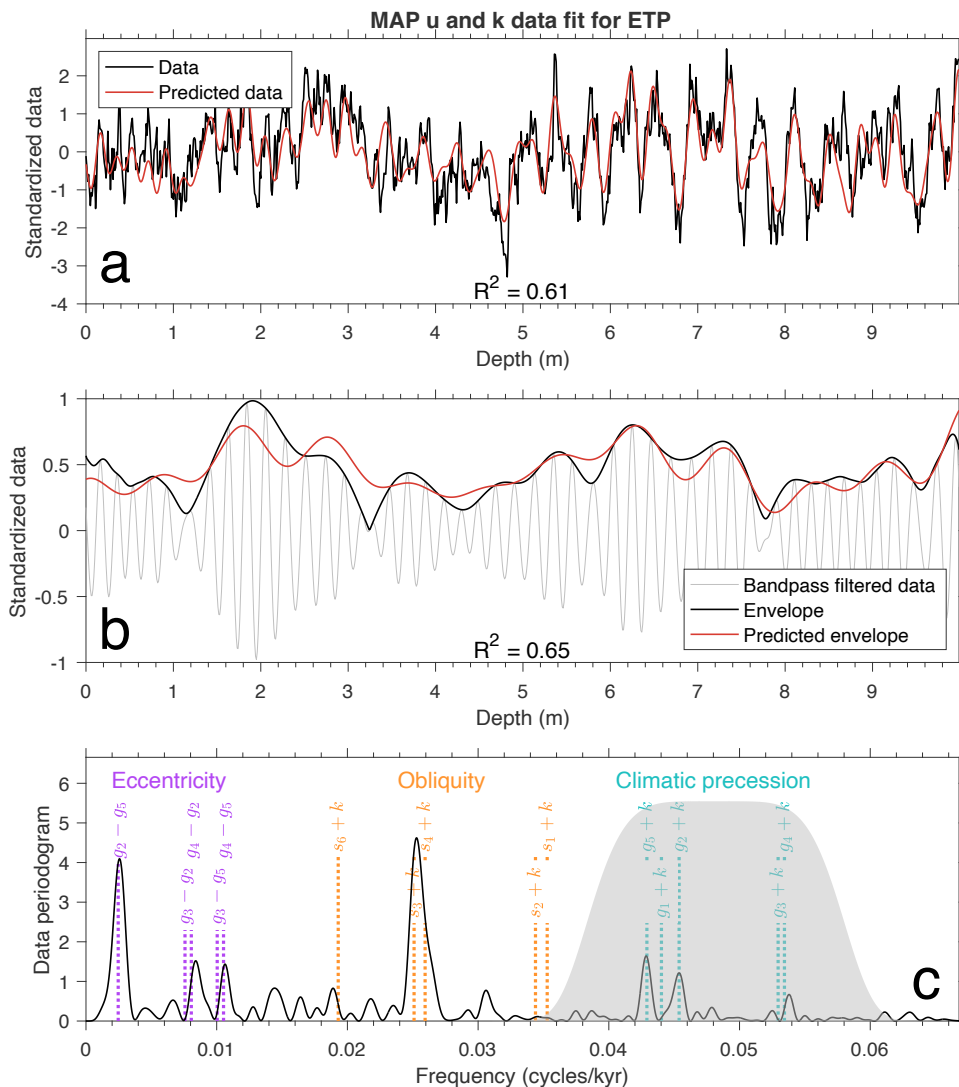
428 The fit to the data and to the precession envelope for the maximum a posteriori (MAP)
 429 value of u and k is shown in Figure 3. The R^2 for the data fit is 0.61, which is greater than the
 430 0.44 value used to construct the synthetic data set. This is due to a small amount of variance in
 431 the added noise being attributed to astronomical cycles. The periodogram of the ETP data
 432 (Figure 3c) shows a close correspondence with the spectral lines of the astronomical cycles.
 433



434
435
436
437
438
439
440

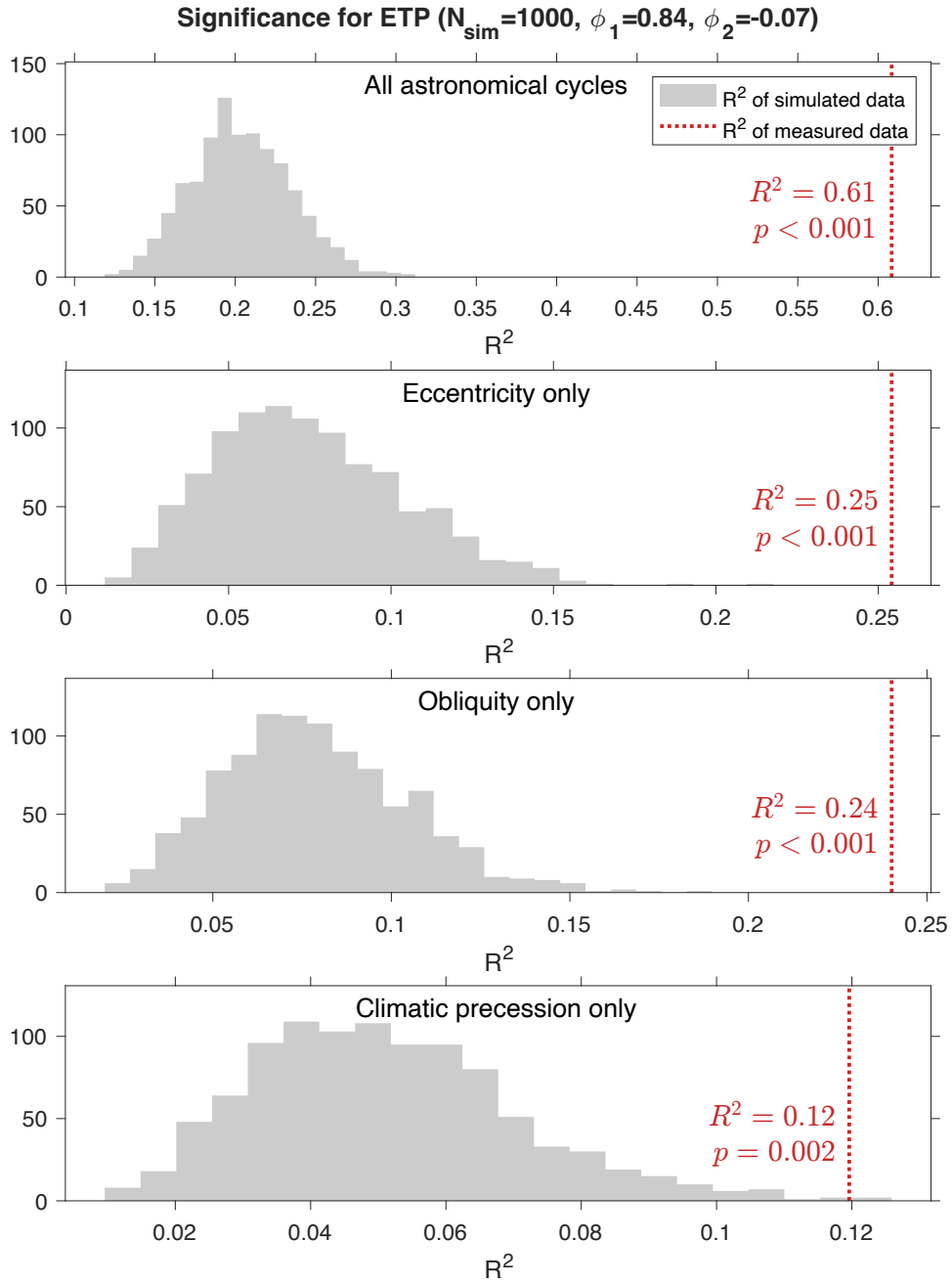
Figure 2. Posterior PDFs of sedimentation rate u and axial precession frequency k obtained by TimeOptB from the synthetic ETP test data set. In the PDF images, the log-posterior PDF is normalized to a MAP value of zero and the posterior PDF to a MAP value of 1. The horizontal dashed line in the posterior PDF image shows the present value of k .

441 To check the significance of the estimated astronomical signals, we generated $N_{\text{sim}} =$
442 1,000 AR(2) time series with coefficients $\phi_1 = 0.84$ and $\phi_2 = -0.07$, equal to those estimated for
443 the MAP value of u and k . The value of these coefficients are close to those of the AR noise that
444 was added to the data ($\phi_1 = 0.8$, $\phi_2 = 0$). Figure 4 shows that the fit to all the astronomical cycles
445 and to each individual set of cycles (climatic precession, obliquity, or eccentricity) is highly
446 significant. Finally, the fit of an AR(2) spectrum to the periodogram of the ETP data, and the
447 sample autocorrelation of the driving noise of the AR(2) process in the residuals e of the spectral
448 fit, are shown in Figure S1. The sample autocorrelation of the driving noise is close to that of
449 white noise, as expected. In conclusion, TimeOptB is successful in recovering the sedimentation
450 rate and axial precession frequency in a synthetic data set contaminated by a realistic amount of
451 correlated noise.



452
453
454
455
456
457
458
459
460

Figure 3. Fit to the synthetic ETP test stratigraphic data for the TimeOptB-derived MAP value of sedimentation rate u (0.994 cm/kyr) and axial precession frequency k (51.357 arcsec/yr). (a) Fit between measured and predicted stratigraphic data (spectral fit). (b) Fit of the bandpassed climatic precession signal (envelope fit). (c) Data periodogram (black continuous line) and frequencies of astronomical cycles (dotted vertical lines). The gray shaded area shows the frequency response of the filter used to compute the bandpassed climatic precession signal in the data (gray curve in (b)).

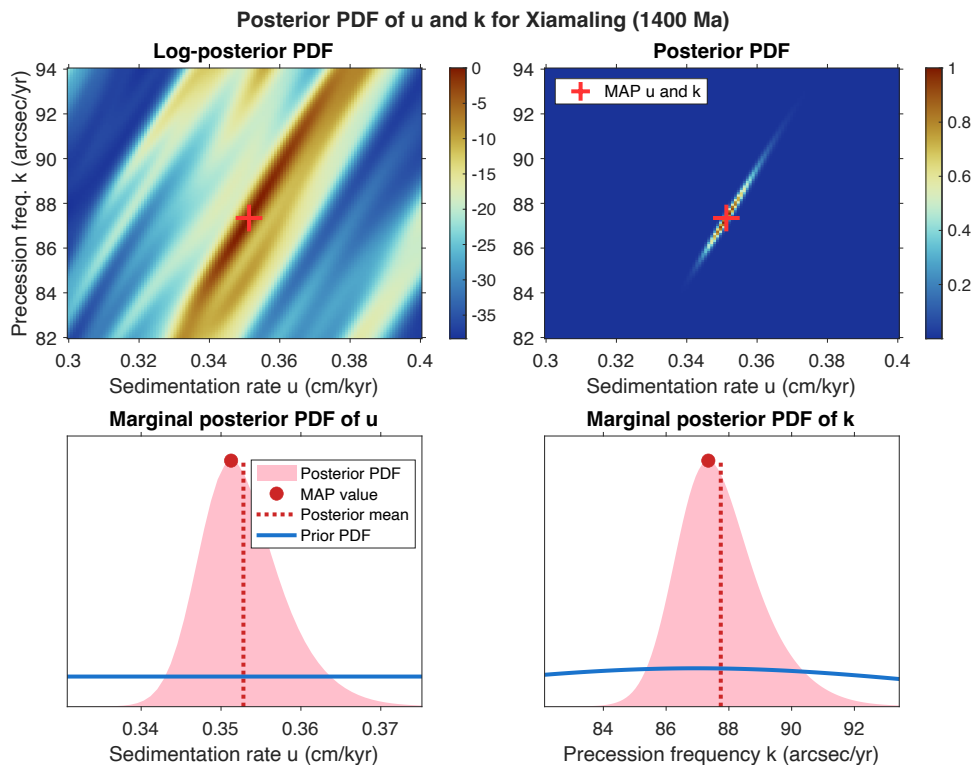


461
462
463
464
465
466
467
468
469

Figure 4. TimeOptB Monte Carlo significance testing for the synthetic ETP data set. The gray histograms show the distribution of TimeOptB R^2 values in $N_{\text{sim}} = 1000$ random AR(2) time series. The R^2 in the random time series matches or exceeds the value obtained for the synthetic ETP data set (red dotted line) at most two times out of 1000 when evaluating climatic precession alone, and does not exceed any of the simulated R^2 values when evaluating obliquity only, eccentricity only, or all of the astronomical cycles together.

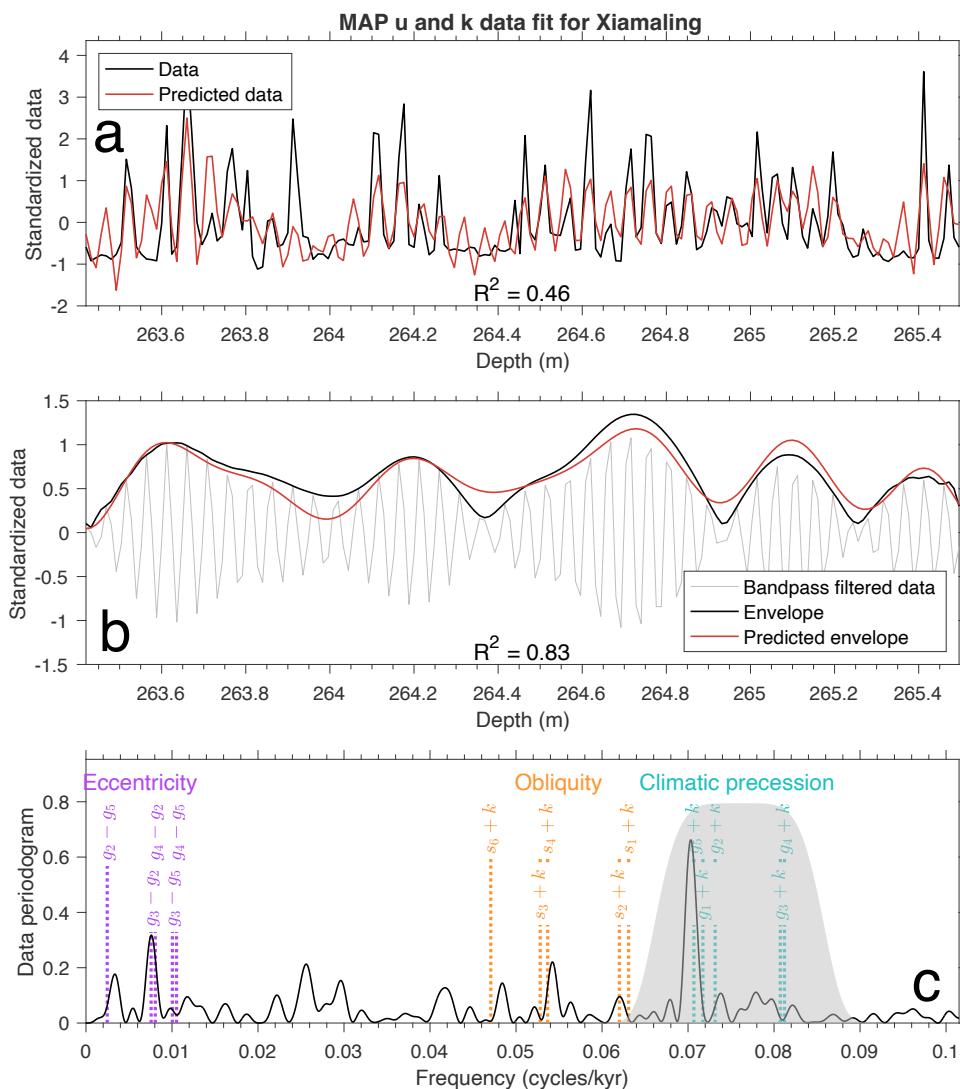
470 **4.2 Xiamaling Formation (1.4 Ga)**

471 We apply the TimeOptB methodology to a published Cu/Al record from the 1.4 Ga
 472 Proterozoic Xiamaling Formation, North China craton (Zhang et al., 2015), one of the data sets
 473 studied by MM18. The data interval is 2 m-thick and spans about 570 kyr (for the posterior mean
 474 sedimentation rate determined below).
 475
 476



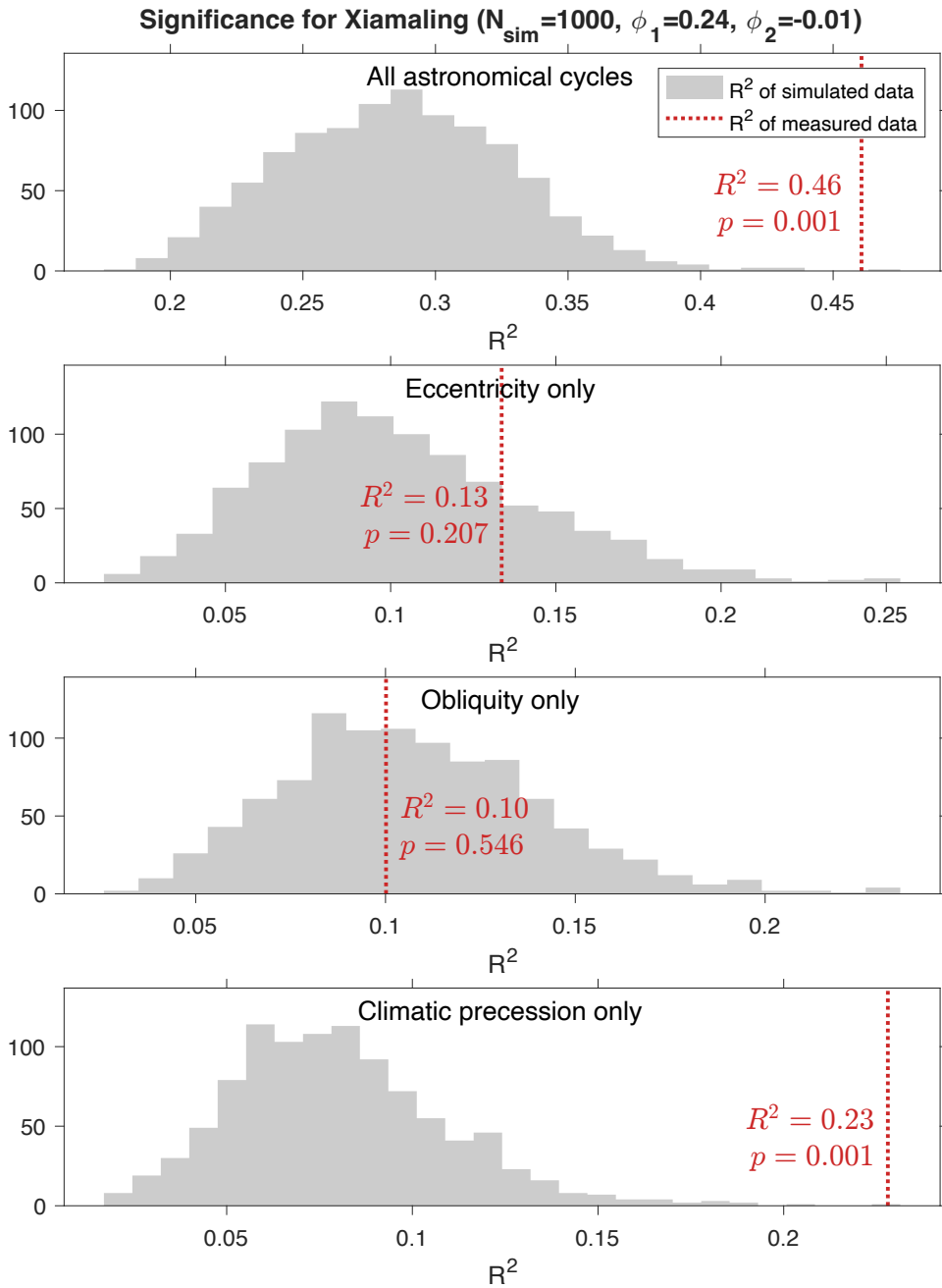
477
 478
 479 **Figure 5.** Posterior PDFs of sedimentation rate u and axial precession frequency k obtained by TimeOptB
 480 from the Xiamaling formation data set. In the PDF images, the log-posterior PDF is normalized to a MAP
 481 value of zero and the posterior PDF to a MAP value of 1.
 482

483 The posterior PDFs of sedimentation rate u and axial precession frequency k are shown in
 484 Figure 5. The prior PDF of k is very broad, reflecting a large uncertainty about k at 1.4 Ga, but
 485 the data are informative and result in a much narrower posterior PDF. The MAP value of u and k
 486 predict data that match closely the precession-modulated climatic precession cycles in the
 487 measured Cu/Al data, and prominent peaks in the data periodogram are near the predicted
 488 frequencies of eccentricity and climatic precession (Figure 6). The results are also consistent
 489 with the presence of an obliquity signal, which was not evaluated in the MM18 TimeOptMCMC
 490 inversion. The Monte Carlo significance experiments in Figure 7 support the presence of
 491 astronomical cycles, with low p -values of 0.001 when all the astronomical cycles are considered
 492 or when only climatic precession is tested. The fit of an AR(2) process to the Xiamaling data is
 493 illustrated in Figure S2, and it confirms that the driving noise of the AR(2) process is nearly
 494 white noise.



495
496
497
498
499
500
501
502
503

Figure 6. Fit to the Xiamaling formation Cu/Al data obtained by TimeOptB for the MAP value of sedimentation rate u and axial precession frequency k (see Table 3). (a) Fit between measured and predicted stratigraphic data (spectral fit). (b) Fit of the bandpassed climatic precession signal (envelope fit). (c) Data periodogram (black continuous line) and frequencies of astronomical cycles (dotted vertical lines). The gray shaded area shows the frequency response of the filter used to compute the bandpassed climatic precession signal in the data (gray curve in (b)).



504
 505
 506
 507
 508
 509
 510
 511

Figure 7. TimeOptB Monte Carlo significance testing for the Xiamaling formation data set. The gray histograms show the distribution of TimeOptB R^2 values in $N_{\text{sim}} = 1000$ random AR(2) time series. The R^2 values in the random time series are all clearly lower than the value obtained for the measured data (red dotted line) when considering all the astronomical cycles or the climatic precession cycles only.

512 **Table 3.** Results of TimeOptB and TimeOptBMCMC for the Xiamaling Formation Cu/Al and Walvis
 513 Ridge a* data.
 514

Xiamaling Formation (1.4 Ga)					
	MAP value	Posterior mean	Posterior σ	95% credible interval	Method
Sedimentation rate u (cm/kyr)	0.351	0.353	0.00540	0.343-0.365	TimeOptB
	0.353	0.352	0.00541	0.343-0.364	TimeOptBMCMC
Axial precession frequency k (arcsec/yr)	87.34	87.74	1.38	85.37-90.81	TimeOptB
	87.82	87.49	1.38	85.21-90.61	TimeOptBMCMC
Semi-major axis of lunar orbit a (Earth radii)		53.08	0.27		From TimeOptB posterior mean and
LOD (hrs)		18.47	0.25		σ
Walvis Ridge (55 Ma)					
	MAP value	Posterior mean	Posterior σ	95% credible interval	Method
Sedimentation rate u (cm/kyr)	1.308	1.309	0.00605	1.297-1.320	TimeOptB
	1.311	1.310	0.00620	1.299-1.322	TimeOptBMCMC
Axial precession frequency k (arcsec/yr)	51.15	51.25	0.29	50.70-51.81	TimeOptB
	51.31	51.29	0.29	50.75-51.85	TimeOptBMCMC
Semi-major axis of lunar orbit a (Earth radii)		60.07	0.20		From TimeOptB posterior mean and
LOD (hrs)		23.75	0.18		σ

515
516

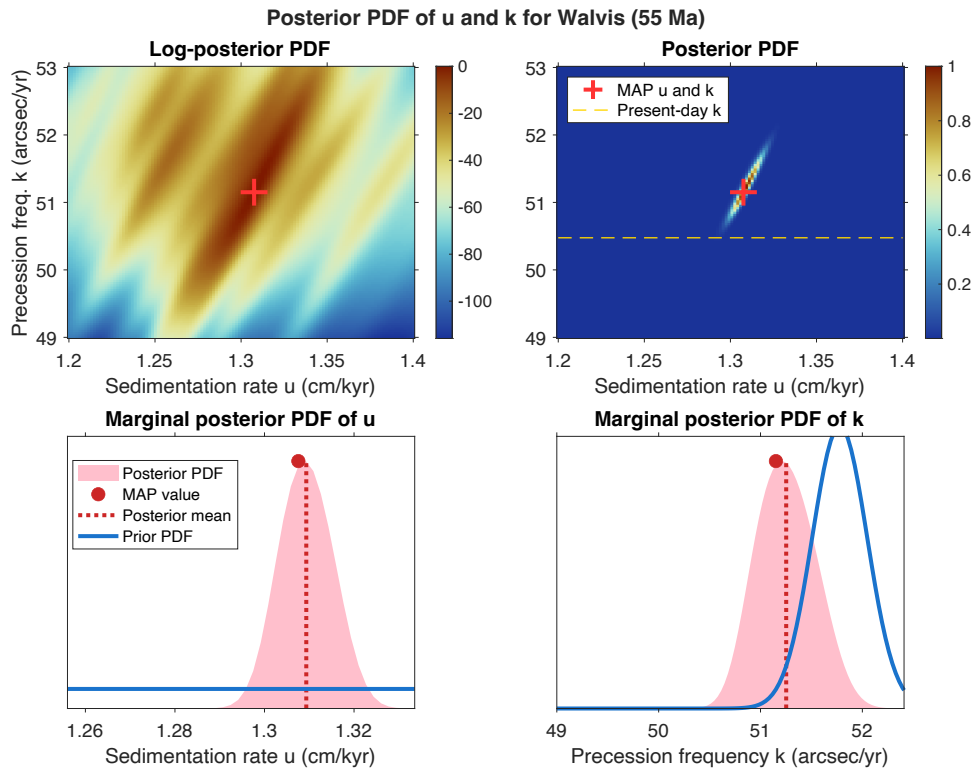
517 **4.3 Walvis Ridge ODP Site 1262 (55 Ma)**

518 Another case study for the TimeOptB methodology uses a record of reflectivity data (a*,
 519 red/green) measured on Eocene-age sediments cored at ODP Site 1262, Walvis Ridge, South
 520 Atlantic (Zachos et al., 2004), which was also studied by MM18. We refer to that study and
 521 Zachos et al. (2004) for details about the a* data set. The data interval is 21 m-thick and spans
 522 about 1.6 Ma (for the posterior mean sedimentation rate determined below).

523 The posterior PDFs of sedimentation rate u and axial precession frequency k are
 524 illustrated in Figure 8. At 55 Ma, the prior PDF of k is much narrower than in the Proterozoic
 525 example; the Walvis Ridge data point to values of k that are somewhat lower than those in the
 526 prior PDF. As in the previous example, the MAP values of u and k result in predicted data that
 527 closely reproduce the observed precession-modulated climatic precession cycles, and the
 528 predicted frequencies of eccentricity and climatic precession coincide with the highest peaks in
 529 the data periodogram (Figure 9). The periodogram of the Walvis record shows very little power
 530 at the expected frequencies of obliquity, and the Monte Carlo significance experiments show
 531 high significance for all astronomical cycles, for eccentricity only, and for climatic precession
 532 only (Figure 10). In contrast, the power of cycles at the obliquity frequencies in the random
 533 simulated data is always greater than in the measured data; the reason is that the obliquity
 534 frequency band (0.019-0.035 cycles/kyr) of the periodogram of the Walvis data has markedly
 535 lower power than that of the fitted AR(2) process (Figure S3a). Figure S3b shows that the
 536 driving noise of the fitted AR(2) process is nearly white noise.

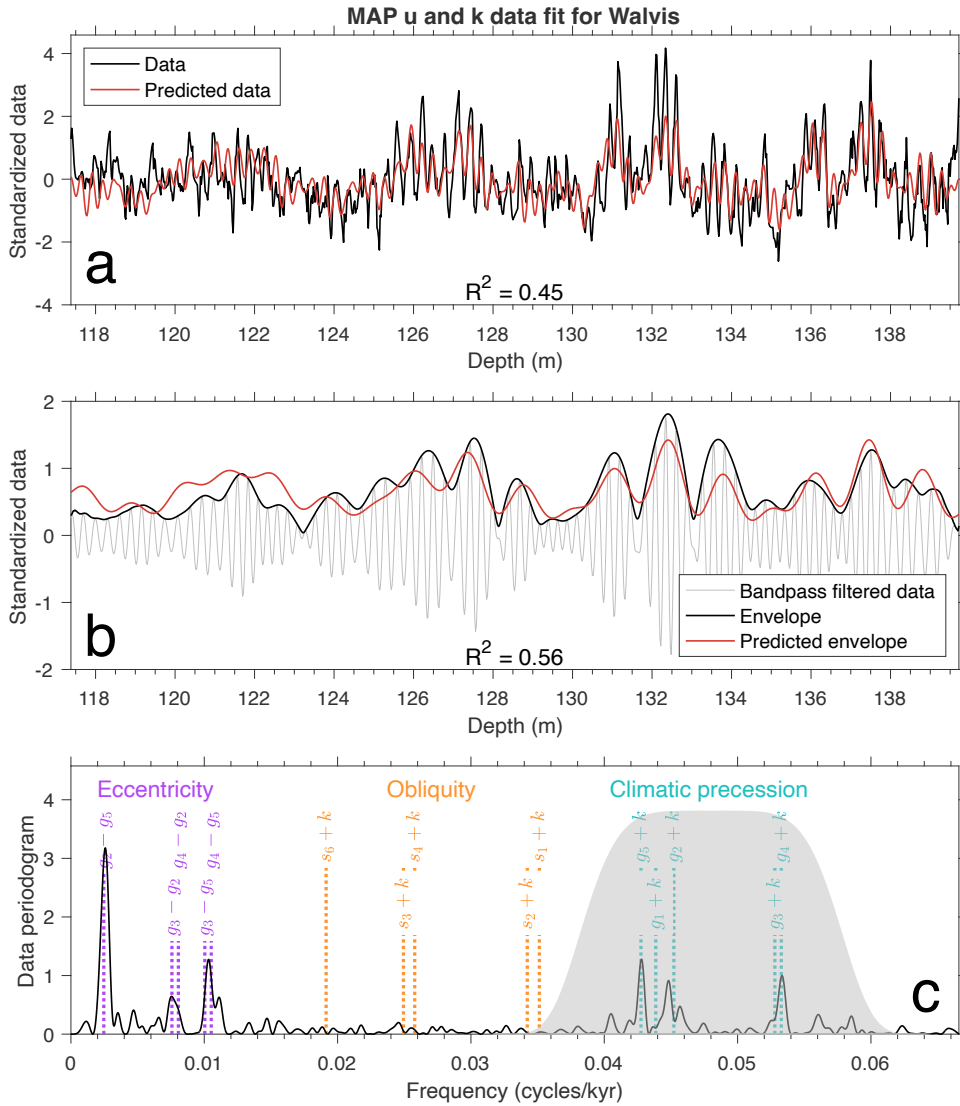
537

538
539



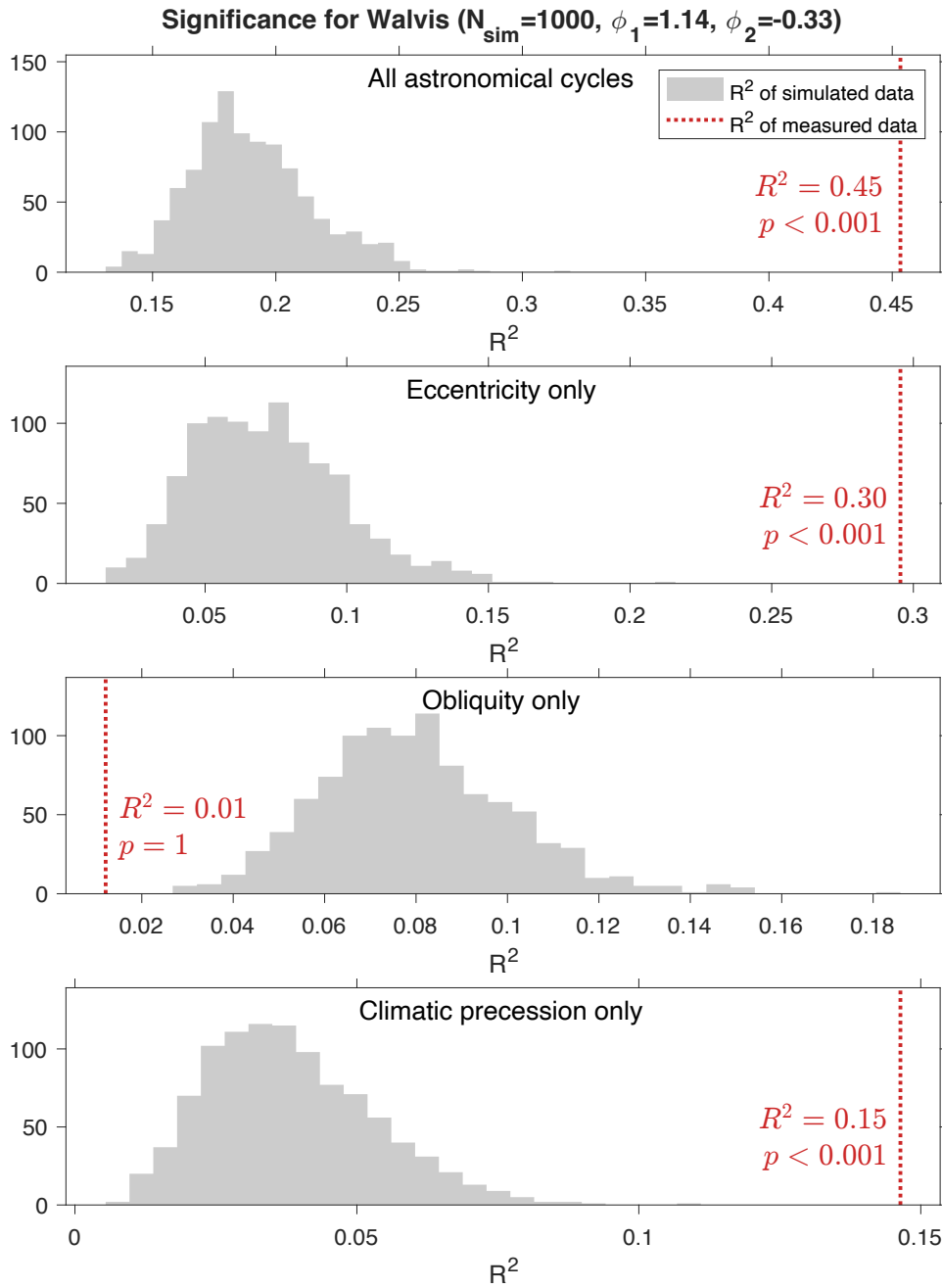
540
541
542
543
544
545
546

Figure 8. Posterior PDFs of sedimentation rate u and axial precession frequency k obtained by TimeOptB from the Walvis Ridge a^* data set. In the PDF images, the log-posterior PDF is normalized to a MAP value of zero and the posterior PDF to a MAP value of 1. The horizontal dashed line in the posterior PDF image shows the present value of k .



547
 548
 549
 550
 551
 552
 553
 554
 555
 556

Figure 9. Fit to the Walvis Ridge a^* data obtained by TimeOptB for the MAP value of sedimentation rate u and axial precession frequency k (see Table 3). (a) Fit between measured and predicted stratigraphic data (spectral fit). (b) Fit of the bandpassed climatic precession signal (envelope fit). (c) Data periodogram (black continuous line) and frequencies of astronomical cycles (dotted vertical lines). The gray shaded area shows the frequency response of the filter used to compute the bandpassed climatic precession signal in the data (gray curve in (b)).



557
558
559
560
561
562
563
564
565

Figure 10. TimeOptB Monte Carlo significance testing for the Walvis Ridge data set. The gray histograms show the distribution of TimeOptB R^2 values in $N_{\text{sim}} = 1000$ random AR(2) time series. The R^2 values in the random time series are clearly lower than the value obtained for the measured data (red dotted line) when considering all the astronomical cycles, the eccentricity cycles only, or the climatic precession cycles only.

566 **5 TimeOptBMCMC methodology**

567 In the TimeOptB method, the only variable parameters are the sedimentation rate u and
 568 axial precession frequency k , while the fundamental Solar system frequencies g_i and s_i are kept
 569 fixed at their prior mean values. As noted in the Introduction, however, we also aim to use
 570 stratigraphic records to constrain the history of variation in the frequencies g_i and s_i and in long-
 571 term astronomical periodicities such as the $g_4 - g_3$ cycle. The method we present here is an
 572 offshoot of the TimeOptMCMC procedure of MM18, which sampled the posterior PDF of five
 573 fundamental Solar system frequencies g_i , axial precession frequency k , and sedimentation rate u
 574 (plus some hyperparameters, discussed below). In TimeOptBMCMC we add the five Solar
 575 system frequencies s_i to determine the posterior PDF of the full twelve-parameter vector in
 576 Equation 1.

577 Whereas in TimeOptB the value of the posterior PDF was calculated systematically over
 578 a grid of two parameters (u and k), the same strategy cannot be used for twelve parameters.
 579 Evaluating the PDF over a grid of M points for each parameter (say, $M = 100$) would require M^{12}
 580 calculations, which is entirely impractical. In contrast, MCMC algorithms perform a random
 581 walk that concentrates on the high-posterior probability region of the parameter space and are
 582 designed to return a sample distributed as in the posterior PDF. General treatments of MCMC in
 583 the statistical literature can be found in Gilks et al. (1996) and Brooks et al. (2011); examples of
 584 applications to geophysical inverse problems are in Malinverno (2002), Sambridge & Mosegaard
 585 (2002), Piana Agostinetti & Malinverno (2010), and Sen & Stoffa (2013).

586 TimeOptBMCMC uses a Metropolis-within-Gibbs algorithm (originally described by
 587 Metropolis et al., 1953): in each step of the random walk, a candidate parameter vector is
 588 obtained by adding to one of the parameters a random value chosen from a proposal PDF (e.g., a
 589 zero-mean normal PDF). The candidate is then accepted with a probability that depends on the
 590 ratio of the posterior PDFs of the candidate and the current parameter vector. This simple
 591 strategy will asymptotically return a sample of parameter vectors distributed as in the posterior
 592 PDF.

593 An outstanding issue in implementing a Metropolis algorithm is how to choose the scale
 594 parameter of the proposal PDF (e.g., the standard deviation of a normal PDF). If this scale is set
 595 too large, most candidates will not be accepted; if too small, the probability of acceptance will be
 596 large but the random walker will diffuse too slowly through the parameter space. In both cases, it
 597 will take a long time to explore the high-posterior probability region. In TimeOptBMCMC, we
 598 apply an adaptive Metropolis-within-Gibbs algorithm (Haario et al., 2001; Roberts & Rosenthal,
 599 2009), where parameters are changed one at a time and the standard deviation of the normal
 600 proposal PDF of each parameter is progressively adjusted from a starting value to maintain a
 601 target rate of acceptance of 0.44, which has been shown to be optimal in this case (Roberts &
 602 Rosenthal, 2001). This is a significant improvement over TimeOptMCMC (MM18), which
 603 required a laborious initial experimentation, running a number of MCMC sampling chains to
 604 adjust the scale parameters of the proposal PDFs, often resulting in acceptance rates that were
 605 not ideal, which increased the computation time.

606 Another key difference is that TimeOptBMCMC applies an empirical Bayes approach to
 607 estimate directly from the data a best value of the hyperparameters that control the form of the
 608 covariance matrix of the residuals in the likelihood function for the spectral fit (two AR process
 609 coefficients and the residual variance; see above). TimeOptMCMC instead characterized the

610 residuals with an AR(1) process, which is not always appropriate (e.g., the spectral fit residuals
 611 in the Walvis Ridge data required a nonzero coefficient ϕ_2 ; see Figure S3), and included the AR
 612 process coefficient and the variance of the residuals as variable hyperparameters in the inversion,
 613 which adds to the computational cost of the MM18 procedure.

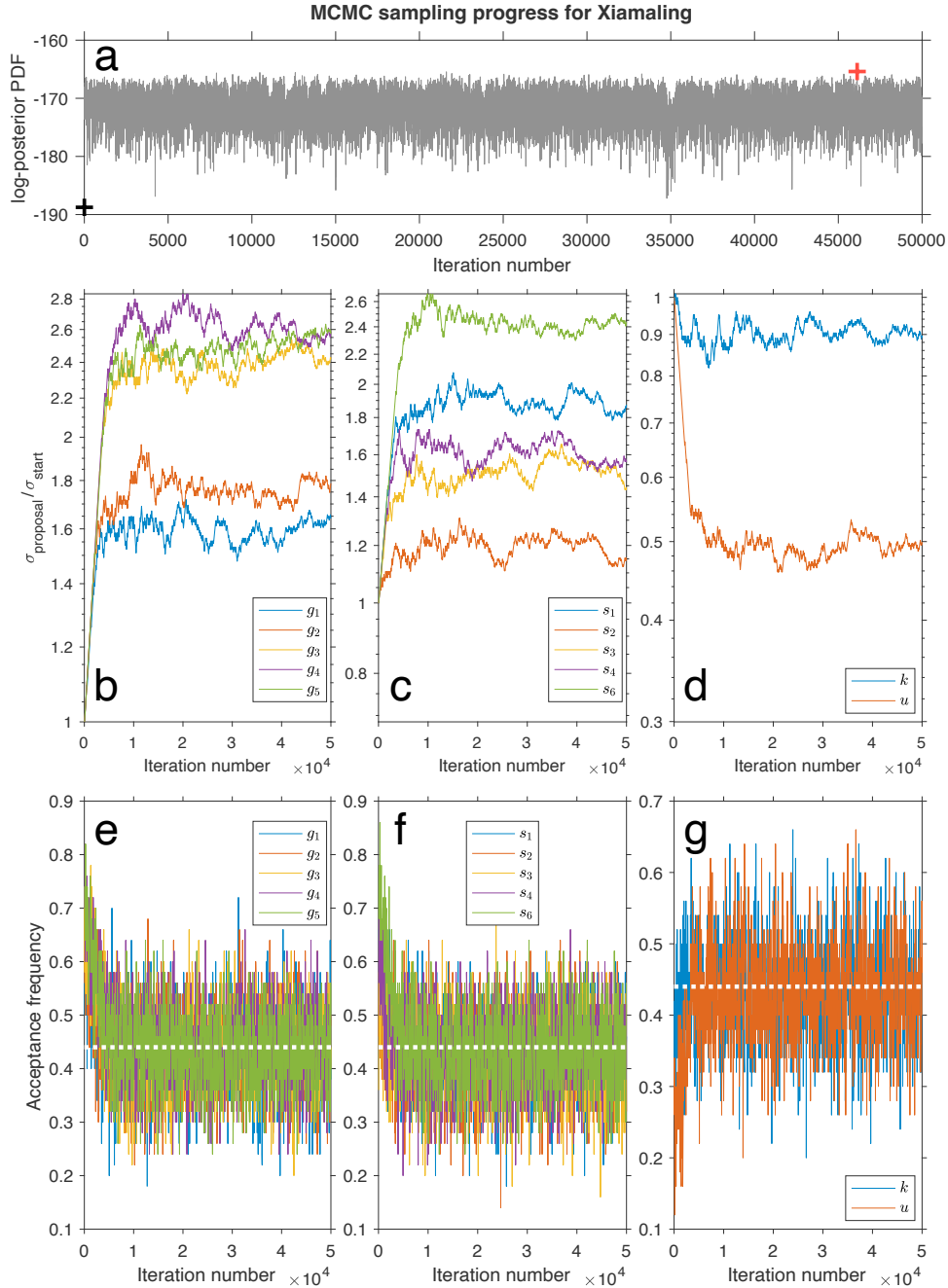
614 **6 TimeOptBMCMC example results**

615 **6.1 Xiamaling Formation (1.4 Ga)**

616 The progress of TimeOptBMCMC in sampling the posterior PDF of all the parameters
 617 for the Xiamaling Cu/Al data is illustrated in Figure 11. The chain is started from the prior mean
 618 value of the Solar system frequencies g_i and s_i , axial precession frequency k , and sedimentation
 619 rate u (whose prior PDF is a uniform distribution between 0.3 and 0.4 cm/kyr) and proceeds for
 620 50,000 iterations. The value of the posterior PDF rises very quickly at the start of the MCMC
 621 sampling chain and then fluctuates within the high-probability region (Figure 11a). The initial
 622 values of the standard deviation of each proposal PDF are set to the prior standard deviation of
 623 the astronomical frequencies (with an upper limit for the proposal standard deviation of k , where
 624 the prior standard deviation can be very large) and to a small fraction of the prior mean of u . The
 625 progressive adjustment of the proposal PDF standard deviations (Figure 11b-d) and the
 626 corresponding change in the frequency of acceptance (Figure 11e-g) show that after about 5,000
 627 iterations the proposal standard deviations and the frequency of acceptance for each parameter
 628 fluctuate around a constant value, with an average frequency of acceptance around the optimal
 629 value of 0.44.

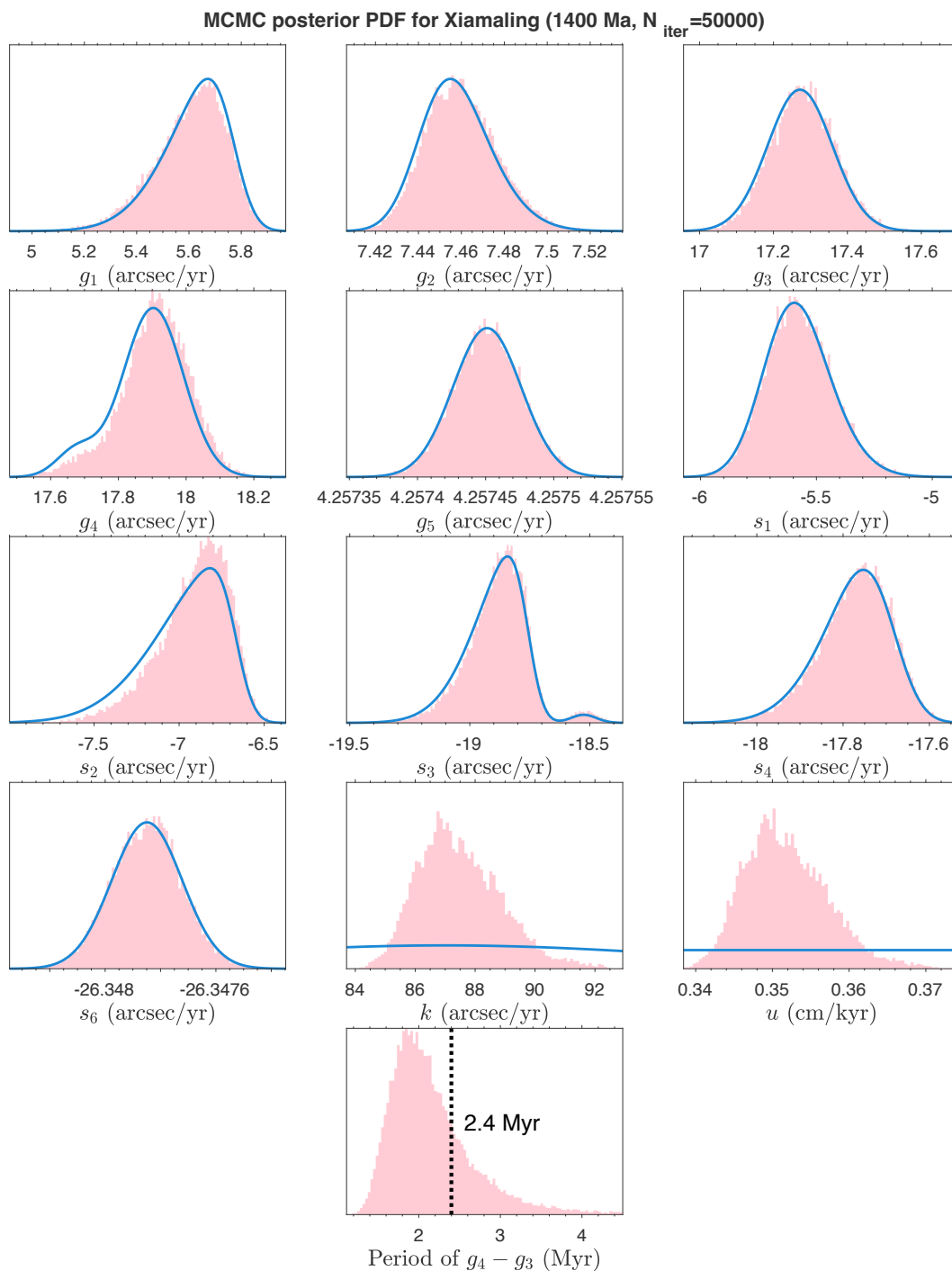
630 Figure 12 compares the prior PDFs of each parameter to the histograms of the values
 631 sampled by TimeOptBMCMC, which approximate each posterior PDF. The prior and posterior
 632 PDFs of the g_i and s_i frequencies are very similar, whereas the data clearly constrain the posterior
 633 values of k and u to a much narrower interval than in the prior PDF. Figure 12 also shows the
 634 posterior histogram of the period corresponding to the $g_4 - g_3$ frequency, which has a sizable
 635 posterior uncertainty (the central 95% interval of the posterior PDF is 1.47-3.78 Myr). The
 636 present day value of the $g_4 - g_3$ period (2.4 Myr) is within the range consistent with the
 637 Xiamaling data at 1.4 Ga.

638 The posterior correlations between the parameters are generally small, with the exception
 639 of a strong positive correlation between u and k (Figure S4), which is the same positive
 640 correlation obtained in the TimeOptB results for the Xiamaling formation Cu/Al data (Figure 5).
 641 The marginal posterior PDFs of u and k obtained by TimeOptB (g_i and s_i fixed to their prior
 642 mean values) and TimeOptBMCMC (g_i and s_i variable) are also very similar (compare Figures 5
 643 and 12 and the posterior PDF statistics in Table 3). Finally, the MAP value of the parameters
 644 sampled by TimeOptBMCMC results in predicted data that are essentially the same as those
 645 obtained by TimeOptB (compare Figures 6 and S5).



646
647

648 **Figure 11.** Progress of TimeOptBMCMC sampling for the Xiamaling formation Cu/Al data set over
649 50,000 iterations. (a) Value of the log-posterior PDF for the sampled model parameter vectors. The black
650 cross is the starting value and the red cross the MAP. (b, c, d) Standard deviation of the proposal PDF (as
651 a ratio over the starting value) for each model parameter. (e, f, g) Frequency of acceptance of the
652 proposed steps in the MCMC random walk. The adaptive Metropolis algorithm used in TimeOptBMCMC
653 adjusts the standard deviations of the proposal PDF to keep the frequency of acceptance around the
654 optimal value of 0.44 for all model parameters (white horizontal dotted line).
655



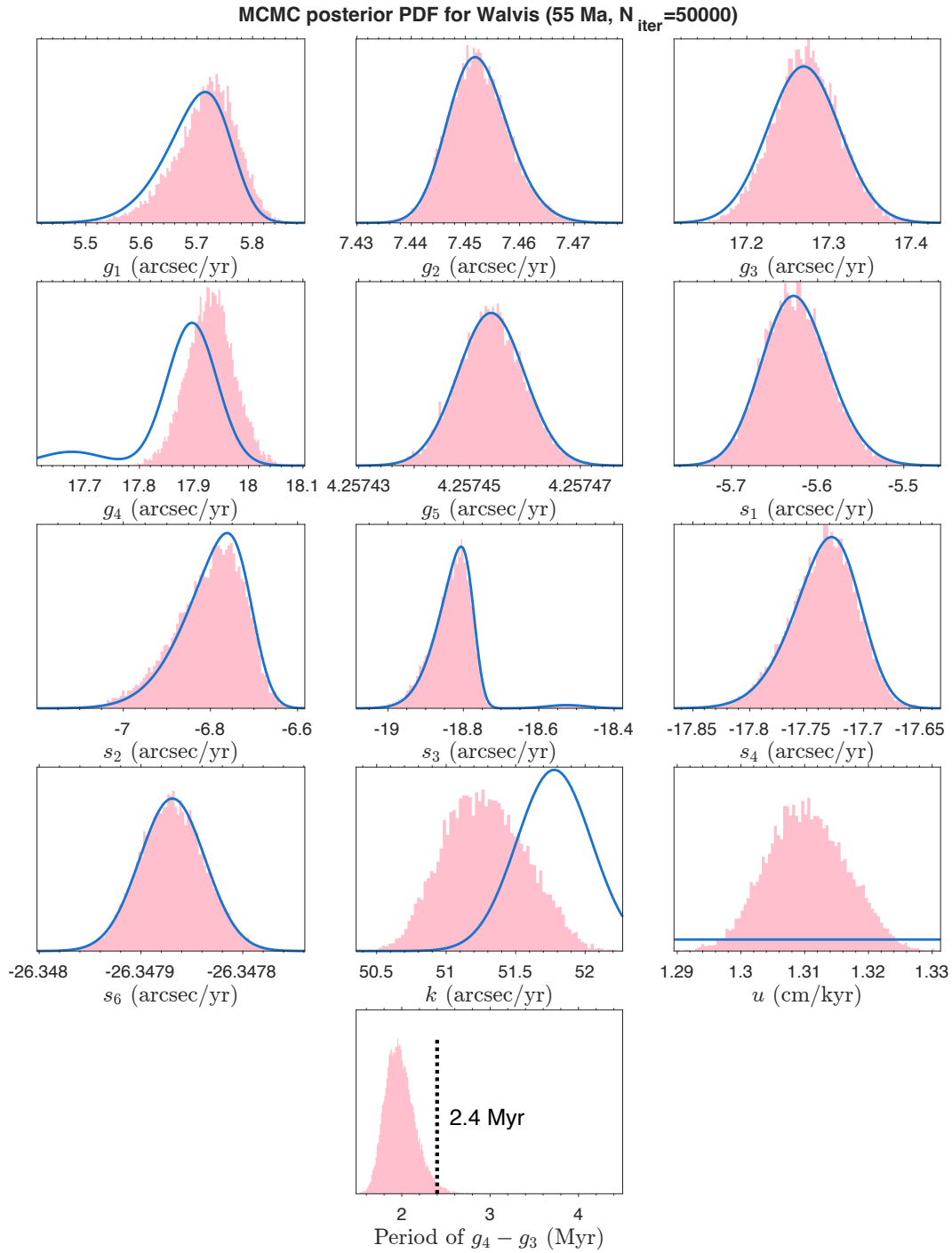
656
657
658
659
660
661
662
663

Figure 12. Histograms of posterior model parameter values sampled by TimeOptBMCMC for the Xiamaling formation Cu/Al data set over 50,000 iterations (light red) compared to the prior PDFs (blue curves). The bottom panel shows the posterior distribution of sampled $g_4 - g_3$ periods compared to the present day value of 2.4 Myr (vertical dotted black line).

664 6.2 Walvis Ridge ODP Site 1262 (55 Ma)

665 The progress of TimeOptBMCMC in sampling the posterior PDF for the Walvis Ridge
666 a* data (Figure S6) is very similar to that seen for the Xiamaling formation Cu/Al data (Figure
667 11). The prior and posterior PDFs of g_i and s_i are also similar, with the exception of g_4 , whose
668 posterior PDF is shifted towards higher frequencies (Figure 13). As a result, the posterior PDF of
669 the $g_4 - g_3$ period is shifted toward shorter periods, and the present day value of 2.4 Myr is in the
670 tail of the posterior PDF (the central 95% interval of the posterior PDF is 1.69-2.38 Myr).

671 As seen for the Xiamaling formation Cu/Al data set, the posterior correlations in the
672 Walvis Ridge a* results are generally small, except for the strong positive correlation between u
673 and k (Figure S7) that was also seen in the TimeOptB results (Figure 8). Again, the marginal
674 posterior PDFs of u and k obtained by TimeOptB (g_i and s_i fixed) and TimeOptBMCMC (g_i and
675 s_i variable) are very similar (compare Figures 8 and 13 and posterior statistics in Table 3). The
676 data predicted by the MAP value obtained by TimeOptB and TimeOptBMCMC are also
677 essentially identical (compare Figures 9 and S8).



678
679
680
681
682
683
684

Figure 13. Histograms of posterior model parameter values sampled by TimeOptBMCMC for the Walvis Ridge formation a* data set over 50,000 iterations (light red) compared to the prior PDFs (blue curves). The bottom panel shows the posterior distribution of sampled $g_4 - g_3$ periods compared to the present day value of 2.4 Myr (vertical dotted black line).

685 **7 Lunar distance and LOD from an estimate of axial precession frequency k**

686 The axial precession frequency k depends on both the lunar distance a (semi-major axis
687 of the Moon orbit) and the Earth spin rate ω (or equivalently, LOD); e.g., see Equation 7 of
688 Berger & Loutre (1994) or Equation 4.14 of Laskar (2020). Therefore, obtaining values of lunar
689 distance and LOD from an estimate of k requires an additional constraint, which is usually
690 provided by the conservation of angular momentum in the Earth-Moon system (e.g., MM18;
691 Lantink et al., 2022).

692 To estimate lunar distance and LOD from k , we apply two equations derived from
693 Equations 6 and 7 of Walker & Zahnle (1986). The first equation gives the relationship between
694 the axial precession frequency k , lunar distance a , and Earth spin rate ω as

$$695 \quad \frac{\omega(t)}{\omega(0)} = \frac{k(t)}{k(0)} \frac{K+1}{K + \left[\frac{a(t)}{a(0)}\right]^{-3}}, \quad (5)$$

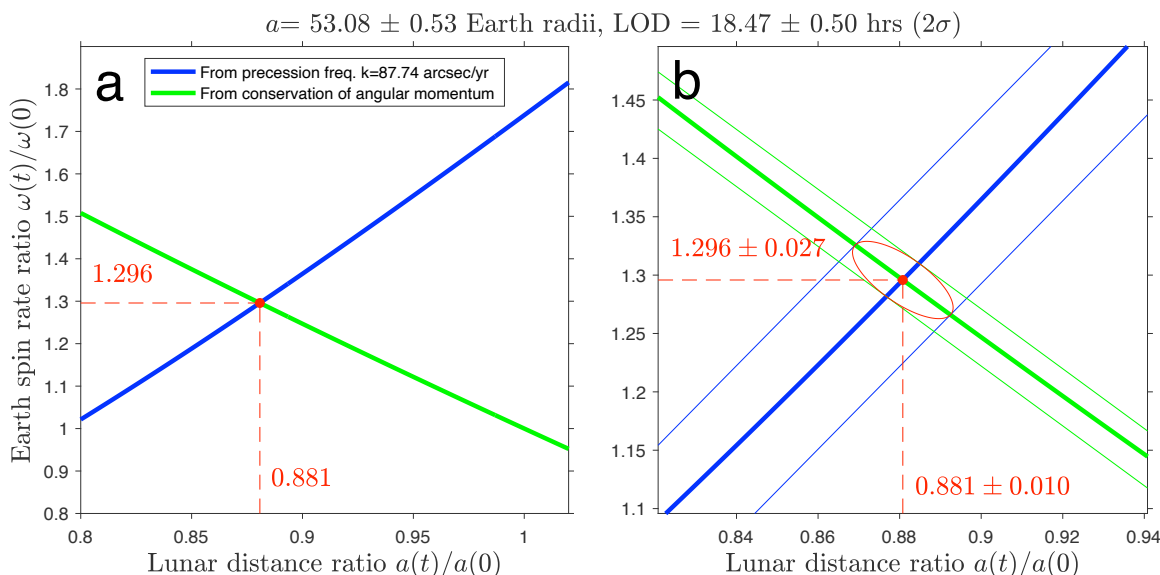
696 where $k(t)/k(0)$, $a(t)/a(0)$, and $\omega(t)/\omega(0)$ are ratios between values at age t and present day values.
697 The second equation is the relationship between lunar distance and LOD that conserves angular
698 momentum in the Earth-Moon system:

$$699 \quad \frac{\omega(t)}{\omega(0)} = 1 + A - A \left[\frac{a(t)}{a(0)}\right]^{1/2}. \quad (6)$$

700 We adjust the values of the constants K and A to account for effects that were originally
701 neglected in Walker & Zahnle (1986): the systematic increase of obliquity ε during geologic time
702 and the slowdown of Earth spin rate due to the effect of solar ocean tides. These adjustments
703 were done by comparing the predictions of Equations 5 and 6 with the values of a , ω , and k
704 calculated over the last 3.3 Ga by Farhat et al. (2022); details are in the Supporting Information.

705 The two relationships above define two curves of $\omega(t)/\omega(0)$ as a function of $a(t)/a(0)$: a
706 “K-curve” that corresponds to a given value of $k(t)/k(0)$ (Equation 5) and an “AM-curve” that
707 conserves angular momentum (Equation 6). The intersection of these two curves, illustrated in
708 Figure 14a, gives the values of past lunar distance a , Earth spin rate ω , and LOD. The
709 Supporting Information describes a simple way to obtain the intersection from a polynomial fit.

710 An uncertainty in the estimates of a and LOD can be calculated on the basis of the
711 uncertainties in the K-curve and AM-curve and of the uncertainty in the value of k estimated
712 from cyclostratigraphic data; see Figure 14b for an illustration and the Supporting Information
713 for details of the calculation. The approach outlined above provides an accurate and quick means
714 to obtain a , LOD, and their uncertainties from an estimate of k , and the results for the examples
715 evaluated here are listed in Table 3.



716
717

718 **Figure 14.** Ratio $\omega(t)/\omega(0)$ between the Earth's spin rate at age t and the present day value as a function
719 of the ratio of the lunar distances $a(t)/a(0)$. (a) The blue curve (K-curve; Equation 5) shows the
720 relationship for the axial precession frequency $k(t)$ estimated from the Xiamaling formation Cu/Al data set
721 ($t = 1.4$ Ga) and the green curve (AM-curve; Equation 6) the relationship that conserves the Earth-Moon
722 angular momentum. The red dot at the intersection of the two curves gives the values of $a(t)/a(0)$ and
723 $\omega(t)/\omega(0)$ at age t . (b) Thin blue and green lines are the 95% contours of normal distributions that describe
724 the uncertainties of the K-curve and AM-curve, respectively, and the red ellipse is the 95% contour that
725 defines the uncertainty of the intersection (see the Supporting Information for details).
726

727 8 Discussion

728 8.1 Estimating axial precession frequency k

729 The case studies evaluated here show that TimeOptB and TimeOptBMCMC are effective
730 in estimating a reliable value for the precession frequency k from stratigraphic data. The key
731 requirement is that the data should display clear eccentricity cycles (which do not depend on k)
732 and clear climatic precession and/or obliquity cycles (which depend on k). The difference in the
733 observed frequencies of eccentricity and those of climatic precession/obliquity allows for
734 estimating k . Thus, to estimate k it is important that sizable astronomical cycles are observed in
735 the periodogram plots for eccentricity and either precession or obliquity (Figures 3, 6, and 9).
736 The TimeOptB significance test should also weed out cases where stratigraphic sequences do not
737 contain significant astronomical cycles (Figures 4, 7, and 10). It should be noted that the methods
738 presented here will not work appropriately if sedimentation rate is not relatively constant within
739 the analyzed stratigraphic interval, which requires careful selection of cyclostratigraphic data sets
740 or portions thereof (more on the sedimentation rate assumption below). Considering these
741 limitations, there should be many stratigraphic data sets that can return reliable estimates of the
742 past axial precession frequency. In addition to providing valuable information on the evolution
743 of lunar distance, LOD, and tidal dissipation, past estimates of k will improve the accuracy of
744 astrochronologies based on climatic precession and obliquity cycles in data.

745 The results in Table 3 supersede those obtained for the Xiamaling formation and Walvis
 746 Ridge in MM18. The differences are minor, and in both cases the posterior PDFs of k and u in
 747 this study overlap with those in MM18. The posterior PDFs of k in the Xiamaling formation are
 748 not identical with MM18 because TimeOptB and TimeOptBMCMC include the fit to obliquity
 749 components, which results in a small increase in k (the posterior mean changes from 85.79
 750 arcsec/yr in MM18 to 87.74 arcsec/yr in Table 3). The posterior PDF of k in the Walvis Ridge
 751 data is very close to that in MM18 even though the prior PDF was different between the studies.

752 The posterior PDFs of u and k obtained by TimeOptB and TimeOptBMCMC are similar
 753 in both the Xiamaling Formation Cu/Al and Walvis Ridge a* data sets (Figures 5, 8, 12, 13, and
 754 Table 3). Thus, in these two case studies, letting the g_i and s_i frequencies be variable parameters
 755 does not lead to different estimates of u and k or to a substantially improved fit of the results
 756 (Figures 6, 9, S5, S8).

757 **8.2 Estimating Solar system fundamental frequencies g_i and s_i**

758 The posterior PDFs of the g_i and s_i frequencies sampled by TimeOptBMCMC are
 759 generally close to the respective priors, with the exception of g_4 in the Walvis Ridge a* data set.
 760 When astronomical cycles are well expressed in the data, this result shows that
 761 TimeOptBMCMC can constrain the values of Solar system fundamental frequencies. The past
 762 Solar system frequencies inferred from stratigraphic data will have inherent uncertainties. In
 763 practice, long-period cycles such as $g_4 - g_3$ will not be reconstructed with high accuracy from
 764 stratigraphic records of relatively short duration, but nonetheless the range of their possible
 765 values can be estimated by TimeOptBMCMC. For example, although the posterior PDF of the g_4
 766 $- g_3$ period in the Walvis Ridge record (55 Ma) spans a broad interval, the results in Figure 13
 767 suggest a $g_4 - g_3$ period that is shorter than the present 2.4 Myr. This result is consistent with the
 768 analysis of Zeebe & Lourens (2019), who found that the Solar system solution that best fit the
 769 Walvis Ridge data displayed a change in the $g_4 - g_3$ period to ~ 1.5 Ma at ages older than 50 Ma.

770 A suggested practical procedure is to run TimeOptB first on a data set, including the
 771 Monte Carlo significance experiments to support the presence of astronomical cycles in the data.
 772 If there is evidence for astronomical cycles in the data, a TimeOptBMCMC run can show
 773 whether the sampled values of the Solar system fundamental frequencies are distributed as in the
 774 prior PDF, meaning that the data are not informative (as in the case of the Xiamaling formation
 775 Cu/Al data set) or whether there are differences from the prior that highlight past variations (as
 776 for g_4 and $g_4 - g_3$ in the Walvis Ridge a* data set).

777 **8.3 Assumption: constant sedimentation rate**

778 A key assumption in TimeOptB and TimeOptBMCMC is that the sedimentation rate was
 779 constant in the studied stratigraphic interval. A preliminary moving window power spectral
 780 analysis or wavelet-based analysis can indicate whether prominent cycles have nearly constant
 781 spatial frequencies as predicted by a constant sedimentation rate. This means that suitable data
 782 sets will likely span a relatively short time interval, and there will be a tradeoff between the need
 783 to have a long enough record of eccentricity cycles and the requirement of a constant
 784 sedimentation rate. Also, the strategy presented here will not be reliable if astronomical signals
 785 are distorted by large cyclic changes in sedimentation rate driven by the effects of particular
 786 astronomical cycles (e.g., Herbert, 1994).

787 Even when sedimentation rate is nearly constant over the interval studied, the examples
 788 presented here show that any error in estimating sedimentation rate u will result in the same error
 789 in axial precession frequency k : a sedimentation rate overestimated by 1% means k will be
 790 overestimated by 1% (see the discussion of the ETP data set results in Figure 2). There is no way
 791 to know k within a small fraction of its value unless the sedimentation rate, or more generally the
 792 time-stratigraphic depth relationship, is also known within that same small fraction. As
 793 stratigraphic data invariably contain variations unrelated to astronomical forcing (“geological
 794 noise;” Meyers, 2019), the time-depth relationship can be determined only approximately. This
 795 is a fundamental issue at the root of cyclostratigraphy and astrochronology applications, and it
 796 cannot be solved by methodological improvements. On the other hand, methods such as those
 797 presented here can quantify the resulting uncertainty and highlight the value and the limitations
 798 of conclusions drawn from the analysis of astronomical cycles in stratigraphic records.

799 **8.4 Assumption: constant Earth-Moon angular momentum**

800 As noted earlier, the axial precession frequency k depends on both lunar distance a and
 801 LOD. Estimating both a and LOD on the basis of k therefore requires an additional constraint,
 802 and therefore we assume that the Earth-Moon angular momentum remained constant throughout
 803 Earth’s history (with a correction due to the small effect of Solar ocean tides in slowing down the
 804 Earth’s rotation).

805 In contrast, Zahnle & Walker (1987) and Bartlett & Stevenson (2016) proposed that when
 806 LOD decreased to ~ 21 hrs in the Proterozoic, a solar atmospheric tide became resonant with the
 807 Earth’s spin rate and counteracted the effect of the lunar ocean tide, maintaining a constant Earth
 808 spin rate for a prolonged duration (between ~ 2 Ga and ~ 1 Ga; Bartlett & Stevenson, 2016).
 809 During this interval, the lunar ocean tide would still have resulted in a torque that moved the
 810 Moon to a higher orbit, so that the total angular momentum of the Earth-Moon system would
 811 have increased through time by as much as 10-20%, extracting angular momentum from the
 812 Earth’s orbit around the Sun (Zahnle & Walker, 1987). Our results give some information on the
 813 possible size of the change in the Earth-Moon angular momentum: taking the value of $k(t)$
 814 estimated from the Xiamaling formation Cu/Al record and a LOD of 21 hours, Equation 5 gives
 815 a ratio $a(t)/a(0) = 0.834$. If the Earth was spinning with a LOD of 21 hrs and the lunar distance
 816 was 83.4% of the present value, the Earth-Moon angular momentum at 1.4 Ga would have been
 817 approximately 95% of the present value.

818 By themselves, estimates of the past axial precession frequency from cyclostratigraphy
 819 will only constrain a combination of lunar distance and LOD, and cannot provide a test of the
 820 constant Proterozoic LOD hypothesis without additional constraints.

821 **9 Conclusions**

822 We presented here two methods, TimeOptB and TimeOptBMCMC, to determine the
 823 frequencies of astronomical cycles in the geologic past recorded by stratigraphic sequences. The
 824 results show a decrease in the Earth’s axial precession frequency from about 88.2 arcsec/year (a
 825 period of 14.7 kyr) in the Proterozoic (1.4 Ga) to 51.2 arcsec/year (25.3 kyr) in the Eocene (55
 826 Ma). Our results imply that at 1.4 Ga Earth days were ~ 18.4 hours long and that the Moon was
 827 12% closer to the Earth compared to the present (assuming that the angular momentum of the
 828 Earth-Moon system was conserved).

829 Stratigraphic data invariably contain “geological noise” unrelated to astronomical
830 forcing, and resultant estimates of astronomical frequencies are inevitably uncertain. By applying
831 a Bayesian formulation, we determine posterior probability distributions that describe how much
832 each astronomical frequency can vary while fitting the observed data. We also describe a Monte
833 Carlo procedure to test whether astronomical cycles are significant over a noisy background of
834 sediment property variations.

835 A key assumption of our methods is that sedimentation rate remains constant in the
836 studied interval. This conservative requirement keeps the analysis simple and ensures that
837 recovered astronomical cycles are not the result of overfitting due to arbitrary changes in
838 sedimentation rate. We plan to investigate relaxing this assumption in future developments, for
839 example using “sedimentation templates” (Meyers, 2019) or age models defined by a number of
840 age-depth tie points (e.g., Haslett & Parnell, 2008). Variations in the age-depth relationship
841 should be kept as small as possible to avoid overfitting, and a sound significance analysis should
842 be performed to avoid artificially identifying astronomical cycles.

843 While the constant sedimentation rate assumption restricts the range of suitable
844 cyclostratigraphic records, the examples shown here demonstrate that relatively short
845 stratigraphic intervals (spanning as little as ~600 kyr) provide reliable estimates of past
846 astronomical frequencies. The methods we presented are well suited to recover from the
847 geological record the history of variation in the Earth’s axial precession frequency, the
848 fundamental Solar system frequencies, and the periods of the resultant astronomical insolation
849 rhythms. The results will be useful to constrain the past history of the Earth-Moon and Solar
850 system, to inform models of past tidal dissipation, and to improve astrochronology estimates,
851 especially those based on climatic precession and obliquity cycles.

852

853 **Acknowledgments**

854 The authors declare no conflict of interest. This work was funded by the Heising-Simons
855 Foundation under grant # 2021-2798 (Malinverno) and grant # 2021-2797 (Meyers). The authors
856 thank the members of the CycloAstro project for valuable feedback throughout the development
857 of this study.

858

859 **Open Research**

860 The Xiamaling Formation Cu/Al data (Zhang et al., 2015) and Walvis Ridge a* data
861 (Zachos et al., 2004) used as examples in this study have been previously published and are also
862 accessible with the function ‘getData’ of the ‘Astrochron’ package for R (Meyers, 2014). The
863 prototype code for the TimeOptB and TimeOptBMCMC analyses presented in this work was
864 created in MATLAB and is being used and tested on additional data by CycloAstro graduate
865 students advised by the authors, whose results have not been yet published. The code will be
866 made available in the ‘Astrochron’ package following publication of additional results and
867 translation into the free statistical software R.

868

869 **References**

- 870 Andersen, N. (1974). On the calculation of filter coefficients for maximum entropy spectral
871 analysis. *Geophysics*, 39(1), 69–72. <https://doi.org/10.1190/1.1440413>
- 872 Bartlett, B. C., & Stevenson, D. J. (2016). Analysis of a Precambrian resonance-stabilized day
873 length. *Geophys. Res. Lett.*, 43, 5716–5724, doi:10.1002/2016GL068912.
- 874 Berger, A., & Loutre, M. F. (1994). Astronomical forcing through geological time. *Spec. Publ.*
875 *Int. Ass. Sediment.*, 19, 15–24.
- 876 Brooks, S., Gelman, A., Jones, G. L., & Meng, X.-L. (2011). *Handbook of Markov Chain Monte*
877 *Carlo*. Boca Raton, Florida: Chapman & Hall/CRC.
- 878 Burg, J. P. (1967). Maximum entropy spectral analysis. Presented at the 37th Annual
879 International Meeting, Society of Exploration Geophysicists, Oklahoma City, Oklahoma.
- 880 Carlin, B. P., & Louis, T. A. (2000). *Bayes and Empirical Bayes Methods for Data Analysis*.
881 Boca Raton, Florida: Chapman and Hall/CRC.
- 882 Casella, G. (1985). An Introduction to Empirical Bayes Data Analysis. *The American*
883 *Statistician*, 39(2), 83–87. <https://doi.org/10.2307/2682801>
- 884 Chatfield, C. (1989). *The Analysis of Time Series: An Introduction*. London: Chapman and Hall.
- 885 Cox, D. R., & Miller, H. D. (1965). *The Theory of Stochastic Processes*. London: Chapman and
886 Hall.
- 887 Darwin, S. G. H. (1898). *The Tides and Kindred Phenomena in the Solar System: The Substance*
888 *of Lectures Delivered in 1897 at the Lowell Institute, Boston, Massachusetts*. London:
889 John Murray.
- 890 Dettmer, J., Molnar, S., Steininger, G., Dosso, S. E., & Cassidy, J. F. (2012). Trans-dimensional
891 inversion of microtremor array dispersion data with hierarchical autoregressive error
892 models. *Geophysical Journal International*, 188(2), 719–734.
893 <https://doi.org/10.1111/j.1365-246X.2011.05302.x>
- 894 Farhat, M., Auclair-Desrotour, P., Boué, G., & Laskar, J. (2022). The resonant tidal evolution of
895 the Earth-Moon distance. *Astron. Astrophys.*, 665, L1. [https://doi.org/10.1051/0004-](https://doi.org/10.1051/0004-6361/202243445)
896 [6361/202243445](https://doi.org/10.1051/0004-6361/202243445)
- 897 Fitzpatrick, R. (2012). *An Introduction to Celestial Mechanics*. Cambridge: Cambridge
898 University Press. <https://doi.org/10.1017/CBO9781139152310>
- 899 Gelman, A. B., Carlin, J. S., Stern, H. S., & Rubin, D. B. (2004). *Bayesian Data Analysis* (2nd
900 ed.). Boca Raton, Florida: Chapman and Hall/CRC.
- 901 Gilks, W. R., Richardson, S., & Spiegelhalter, D. J. (1996). *Markov chain Monte Carlo in*
902 *practice*. London: Chapman and Hall.
- 903 Haario, H., Saksman, E., & Tamminen, J. (2001). An adaptive Metropolis algorithm. *Bernoulli*,
904 7(2), 223–242.
- 905 Hacking, I. (2001). *An Introduction to Probability and Inductive Logic*. Cambridge: Cambridge
906 University Press.
- 907 Haslett, J., & Parnell, A. (2008). A simple monotone process with application to radiocarbon-
908 dated depth chronologies. *Journal of the Royal Statistical Society: Series C (Applied*
909 *Statistics)*, 57(4), 399–418. <https://doi.org/10.1111/j.1467-9876.2008.00623.x>
- 910 Hays, J. D., Imbrie, J., & Shackleton, N. J. (1976). Variations in the Earth's orbit: Pacemaker of
911 the Ice Ages. *Science*, 194, 1121–1132.
- 912 Herbert, T. D. (1994). Reading orbital signals distorted by sedimentation: Models and examples.
913 *Spec. Publ. Int. Ass. Sediment.*, 19, 483–507.

- 914 Hinnov, L. A. (2013). Cyclostratigraphy and its revolutionizing applications in the earth and
 915 planetary sciences. *GSA Bulletin*, *125*(11–12), 1703–1734.
 916 <https://doi.org/10.1130/B30934.1>
- 917 Hoang, N. H., Mogavero, F., & Laskar, J. (2021). Chaotic diffusion of the fundamental
 918 frequencies in the Solar System. *Astronomy & Astrophysics*, *654*, A156.
 919 <https://doi.org/10.1051/0004-6361/202140989>
- 920 Lantink, M. L., Davies, J. H. F. L., Ovtcharova, M., & Hilgen, F. J. (2022). Milankovitch cycles
 921 in banded iron formations constrain the Earth–Moon system 2.46 billion years ago.
 922 *Proceedings of the National Academy of Sciences*, *119*(40), e2117146119.
 923 <https://doi.org/10.1073/pnas.2117146119>
- 924 Laskar, J. (2020). Chapter 4 - Astrochronology. In F. M. Gradstein, J. G. Ogg, M. D. Schmitz, &
 925 G. M. Ogg (Eds.), *Geologic Time Scale 2020* (pp. 139–158). Elsevier.
 926 <https://doi.org/10.1016/B978-0-12-824360-2.00004-8>
- 927 Laskar, J., Robutel, P., Joutel, F., Gastineau, M., Correia, A. C. M., & Levrard, B. (2004). A
 928 long-term numerical solution for the insolation quantities of the Earth. *Astron.*
 929 *Astrophys.*, *428*, 261–285.
- 930 Ma, C., Meyers, S. R., & Sageman, B. B. (2017). Theory of chaotic orbital variations confirmed
 931 by Cretaceous geological evidence. *Nature*, *542*(7642), 468–470.
 932 <https://doi.org/10.1038/nature21402>
- 933 Malinverno, A. (2002). Parsimonious Bayesian Markov chain Monte Carlo inversion in a
 934 nonlinear geophysical problem. *Geophys. J. Int.*, *151*, 675–688.
 935 <https://doi.org/10.1046/j.1365-246X.2002.01847.x>
- 936 Malinverno, A., & Briggs, V. A. (2004). Expanded uncertainty quantification in inverse
 937 problems: Hierarchical Bayes and empirical Bayes. *Geophysics*, *69*, 1005–1016.
 938 <https://doi.org/10.1190/1.1778243>
- 939 Mann, M. E., & Lees, J. M. (1996). Robust estimation of background noise and signal detection
 940 in climatic time series. *Climatic Change*, *33*, 409–445.
- 941 Metropolis, N., Rosenbluth, A. W., Rosenbluth, M. N., Teller, A. H., & Teller, E. (1953).
 942 Equation of state calculations by fast computing machines. *J. Chem. Phys.*, *21*, 1087–
 943 1092.
- 944 Meyers, S. R. (2014). Astrochron: An R Package for Astrochronology. Retrieved from
 945 <https://cran.r-project.org/package=astrochron>
- 946 Meyers, S. R. (2015). The evaluation of eccentricity-related amplitude modulation and bundling
 947 in paleoclimate data: An inverse approach for astrochronologic testing and time scale
 948 optimization. *Paleoceanography*, *30*(12), 1625–1640.
 949 <https://doi.org/10.1002/2015PA002850>
- 950 Meyers, S. R. (2019). Cyclostratigraphy and the problem of astrochronologic testing. *Earth-*
 951 *Science Reviews*, *190*, 190–223. <https://doi.org/10.1016/j.earscirev.2018.11.015>
- 952 Meyers, S. R., & Malinverno, A. (2018). Proterozoic Milankovitch cycles and the history of the
 953 solar system. *Proc. Nat. Acad. Sci.*, *115*, 6363–6368.
 954 <https://doi.org/10.1073/pnas.1717689115>
- 955 Meyers, S. R., & Peters, S. E. (2022). Exploring the depths of Solar System evolution.
 956 *Proceedings of the National Academy of Sciences*, *119*(43), e2216309119.
 957 <https://doi.org/10.1073/pnas.2216309119>
- 958 Milanković, M. (1941). *Canon of insolation and the ice-age problem: (Kanon der*
 959 *Erdbestrahlung und seine Anwendung auf das Eiszeitenproblem) Belgrade, 1941.*

- 960 Jerusalem: Israel Program for Scientific Translations; [available from U.S. Department of
961 Commerce, Clearinghouse for Federal Scientific and Technical Information, Springfield,
962 Va.].
- 963 Neal, R. N. (1993). *Probabilistic inference using Markov chain methods* (Technical Report
964 CRG-TR-93-1). Department of Computer Science, University of Toronto. Retrieved from
965 <https://www.cs.toronto.edu/~radford/ftp/review.pdf>
- 966 Olsen, P. E., Laskar, J., Kent, D. V., Kinney, S. T., Reynolds, D. J., Sha, J., & Whiteside, J. H.
967 (2019). Mapping Solar System chaos with the Geological Orrery. *Proceedings of the*
968 *National Academy of Sciences*, *116*(22), 10664–10673.
969 <https://doi.org/10.1073/pnas.1813901116>
- 970 Pälike, H., Laskar, J., & Shackleton, N. J. (2004). Geologic constraints on the chaotic diffusion
971 of the Solar System. *Geology*, *32*, 929–932. <https://doi.org/10.1130/G20750.1>
- 972 Piana Agostinetti, N., & Malinverno, A. (2010). Receiver function inversion by trans-
973 dimensional Monte Carlo sampling. *Geophys. J. Int.*, *181*, 858–872.
974 <https://doi.org/10.1111/j.1365-246X.2010.04530.x>
- 975 Priestley, M. B. (1981). *Spectral Analysis and Time Series*. New York: Academic Press.
- 976 Roberts, G. O., & Rosenthal, J. S. (2001). Optimal Scaling for Various Metropolis-Hastings
977 Algorithms. *Statistical Science*, *16*(4), 351–367.
- 978 Roberts, G. O., & Rosenthal, J. S. (2009). Examples of Adaptive MCMC. *Journal of*
979 *Computational and Graphical Statistics*, *18*(2), 349–367.
980 <https://doi.org/10.1198/jcgs.2009.06134>
- 981 Sambridge, M., & Mosegaard, K. (2002). Monte Carlo methods in geophysical inverse problems.
982 *Rev. Geophys.*, *40*(3), 1009. <https://doi.org/10.1029/2000RG000089>
- 983 Sen, M. K., & Stoffa, P. L. (2013). *Global Optimization Methods in Geophysical Inversion* (2nd
984 ed.). Cambridge, New York: Cambridge University Press.
- 985 Ulrych, T. J., & Bishop, T. N. (1975). Maximum entropy spectral analysis and autoregressive
986 decomposition. *Reviews of Geophysics*, *13*(1), 183–200.
987 <https://doi.org/10.1029/RG013i001p00183>
- 988 Walker, J. C. G., & Zahnle, K. J. (1986). Lunar nodal tide and distance to the Moon during the
989 Precambrian. *Nature*, *320*, 600–602.
- 990 Waltham, D. (2015). Milankovitch Period Uncertainties and Their Impact On Cyclostratigraphy.
991 *Journal of Sedimentary Research*, *85*(8), 990–998. <https://doi.org/10.2110/jsr.2015.66>
- 992 Weedon, G. P. (2022). Problems with the current practice of spectral analysis in
993 cyclostratigraphy: Avoiding false detection of regular cyclicity. *Earth-Science Reviews*,
994 *235*, 104261. <https://doi.org/10.1016/j.earscirev.2022.104261>
- 995 Zachos, J. C., Kroon, D., Blum, P., & others. (2004). *Proc. ODP, Init. Repts.*, *208*. College
996 Station, TX: Ocean Drilling Program.
- 997 Zahnle, K., & Walker, J. C. G. (1987). A constant daylength during the Precambrian era?
998 *Precambrian Res.*, *37*, 95–105.
- 999 Zeebe, R. E., & Lourens, L. J. (2019). Solar System chaos and the Paleocene–Eocene boundary
1000 age constrained by geology and astronomy. *Science*, *365*(6456), 926–929.
1001 <https://doi.org/10.1126/science.aax0612>
- 1002 Zeeden, C., Kaboth, S., Hilgen, F. J., & Laskar, J. (2018). Taner filter settings and automatic
1003 correlation optimisation for cyclostratigraphic studies. *Computers & Geosciences*, *119*,
1004 18–28. <https://doi.org/10.1016/j.cageo.2018.06.005>

- 1005 Zhang, S., Wang, X., Hammarlund, E. U., Wang, H., Costa, M. M., Bjerrum, C. J., et al. (2015).
1006 Orbital forcing of climate 1.4 billion years ago. *Proceedings of the National Academy of*
1007 *Sciences*, *112*(12), E1406–E1413. <https://doi.org/10.1073/pnas.1502239112>
- 1008 Zięba, A. (2010). Effective Number of Observations and Unbiased Estimators of Variance for
1009 Autocorrelated Data - an Overview. *Metrology and Measurement Systems*, *17*(1), 3–16.
1010 <https://doi.org/10.2478/v10178-010-0001-0>
- 1011 Zięba, A., & Ramza, P. (2011). Standard Deviation of the Mean of Autocorrelated Observations
1012 Estimated with the Use of the Autocorrelation Function Estimated From the Data.
1013 *Metrology and Measurement Systems*, *18*(4), 529–542. [https://doi.org/10.2478/v10178-](https://doi.org/10.2478/v10178-011-0052-x)
1014 [011-0052-x](https://doi.org/10.2478/v10178-011-0052-x)
- 1015